Journal of Sailing Technology 2025, volume 10, issue 1, pp. 206 - 238.
The Society of Naval Architects and Marine Engineers.

Equivalent Beam Finite Element Model to Assess the Mechanical Behavior of a Composite Hydrofoil

Antoine Faye
Naval Academy Research Institute, France, antoine.faye@ecole-navale.fr.

Alain Nême
ENSTA Bretagne, France.

Frédéric Hauville
Naval Academy Research Institute, France.

Matthieu Sacher
ENSTA, France.

Jean-Baptiste Leroux
ENSTA, France.

David Gross
K-Epsilon, France.

Manuscript received June 5, 2025; revision received August 1, 2025; accepted August 18, 2025.

Abstract. This paper presents and validates a method to model the static structural behavior of composite hydrofoils with 1D beam finite elements. Classically, 3D solid and 2D shell finite elements are employed to predict the anisotropic and heterogeneous behaviors of composite hydrofoils. Modeling a hydrofoil with 1D beam elements drastically reduces its number of structural parameters and the computational time required for the finite element analysis. The present study investigates the static structural behavior of four hydrofoils, constructed in the same mold with different mechanical properties, leading to a specific bend-twist coupling for each foil. The static deformations of the foils are evaluated experimentally and numerically for different load cases. Two numerical models are considered, one with 3D solid and 2D shell elements and a second with 1D beam elements. Then, the results are compared to assess the validity of the 1D finite element model. The comparisons shows that both numerical models are in good agreement with the experimental results. The results also confirm that the 1D finite element model is able to correctly describe the impact of the fiber orientations on the structural responses of the hydrofoils. The computational time savings allowed by the 1D model are also quantified.

Keywords: Hydrofoil; Equivalent Beam; Laminate; Composite; Bend-Twist Coupling; Non-destructive testing; Section analysis.

NOMENCLATURE

$\boldsymbol{B_b}$	Strain-displacement matrix of a beam element [-, m^{-1}]
$\boldsymbol{C}$	Corner of the clamping beam
$\boldsymbol{c_i}$	Orientation of the clamping beam [-]
$\boldsymbol{c_i^k}$	Estimated orientation of the clamping beam at iteration k [-]
$\boldsymbol{D}$	Matrix constraining the warping displacement constitutive matrix [-, m]
Dy, Rx, Rz	Displacement and rotation of the corner of the clamping beam [-, m]

Dx^{warp}	Warping displacements along X [m]
Dy^{warp}	Warping displacements along Y [m]
Dz^{warp}	Warping displacements along Z [m]
E	Young modulus of isotropic material [Pa]
E_1, E_2	Young modulus along longitudinal and transversal directions [Pa]
$\boldsymbol{E_1}$, $\boldsymbol{E_2}$, $\boldsymbol{E_3}$	Frame used to express the equivalent properties of a cross-section [-]
f_1	First eigenfrequency [Hz]
G_{12}, G_{13}, G_{23}	Shear moduli for orthotropic material [Pa]
$\boldsymbol{g}$	Warping contribution to the displacement field [m]
$\boldsymbol{g}^e$	Acceleration of gravity [m s^{-2}]
$\boldsymbol{K}$	Cross-section Timoshenko stiffness matrix [N, N m, N m^{2}]
$\boldsymbol{K_b}$	Stiffness matrix of a beam element [N, N m, N m^{-1}]
$\boldsymbol{K_g}$	Global stiffness matrix [N, N m, N m^{-1}]
L_b	Length of a beam element [m]
L_{ref}	Reference length considered for the GOM-SCAN acquisition [m]
n_p	Number of points used to acquire a face of the clamping beam [-]
n_t	Number of acquisition realized to compute uncertainties [-]
N_b	Number of beam elements [-]
N_1, N_2	Shape functions of a beam element [-]
$\boldsymbol{N}$	Shape functions of the cross-section [-]
$\boldsymbol{Q}$	Material constitutive matrix [Pa]
$\boldsymbol{r}$	Translation and rotation of a cross-section [-, m]
$\boldsymbol{S}$	Cross-section Timoshenko compliance matrix [N^{-1}, N^{-1} m^{-1}, N^{-1} m^{-2}]
$\boldsymbol{T}$	Corner of the clamping
$\boldsymbol{t_i}$	Orientation of the clamping [-]
$\boldsymbol{t_i^k}$	Estimated orientation of the clamping at iteration k [-]
$\boldsymbol{TC}$	Vector connecting the clamping to the corner of the clamping beam [m]
$\boldsymbol{T^kC^k}$	Estimated vector connecting the clamping to the corner of the clamping beam at iteration k [m]
T_{end}	End time of the quasi-staic FEA [s]
T_0, T_{min}	Initial and minimal value of the time step for a quasi-staic FEA [s]
$\boldsymbol{u}$	Nodal displacements of a discretized cross-section [m]
u_i	Displacement of a point of the beam along the direction i [m]
u_i^1, u_i^2	Displacements of the nodes constituting a beam element along the direction i [m]
$\boldsymbol{v}$	Displacement field in a cross-section [m]
$\boldsymbol{w}$	Rigid body motion contribution to the displacement field [m]
x, y, z	Coordinated of a point of a cross-section [m]
X, Y, Z	Point of application of the concentrated load [m]
x^{cis}, y^{cis}	Coordinates of the shear center of a section [m]
$\boldsymbol{y}$	Vertical direction [-]
$\boldsymbol{Z}$	Matrix relating the rotation of the section to the displacement of an arbitrary point [-]
$\boldsymbol{\gamma}$	Translational strain vector [-]
δx, δr	Final uncertainty on the position and rotation [-, m]
δx_i, δr_i	Averaged uncertainty on the position and rotation [-, m]
δx_i^k, δr_i^k	Uncertainty on the position and rotation at iteration k [-, m]
$\boldsymbol{\epsilon}$,	Small strains tensor [-]
ϵ_c, ϵ_t	Gaussian noise associated to the acquisition of the clamping and the clamping beam [-]
$\boldsymbol{\zeta}$	Rigid translation of a cross-section [m]
θ_i	Rotation of a point of the beam around the direction i [-]
θ_i^1, θ_i^2	Rotations of the nodes constituting a beam element around the direction i [-]

$\boldsymbol{\theta}$	Generalized section forces [N,N m]
$\boldsymbol{\kappa}$	Curvature vector [m^{-1}]
ν	Poisson coefficients of isotropic materials [-]
ν_{12}	Poisson coefficients of orthotropic materials [-]
ξ	Local adimensional variable describing the position along a beam element [-]
ρ	Density [kg/m^3]
$\boldsymbol{\sigma}$	Stress tensor [Pa]
χ	Rigid rotation of a cross-section [-]
$\boldsymbol{\Psi}$	Strain-curvature vector [-, m^{-1}]

AoA	Angle of Attack
AR	Aspect Ratio
BTC	Bend-Twist Coupling
CFD	Computational Fluid-Dynamics
DIC	Digital Image Correlation
DoF	Degree of Freedom
FEA	Finite Element Analysis
FEM	Finite Element Method
FSI	Fluid-Structure Interactions
MPC	Multi-Point Constraint
QS	Quasi-Static
UD	Unidirectional

1 INTRODUCTION

Hydrofoils are increasingly adopted in competitive yacht racing, allowing a significant improvement of the ships' performances. To predict their performances, numerical simulations are realized to avoid prototyping (Cella et al., 2021). For example, several studies have been conducted to optimize the shape of the AC75's hydrofoils (Tannenberg et al., 2023; Ng et al., 2025).

For flexible hydrofoils, Fluid-Structure Interactions (FSI) simulations are mandatory since hydrofoil deformations are significant and their impact on the flow cannot be neglected (Balze et al., 2017). FSI simulations require to model coupled problems where both flow and structural responses are solved (Horel and Durand, 2019). For instance, the structural response of a foil can be predicted with the Finite Element Method (FEM) and the flow can be modeled with standard Computational Fluid Dynamics (CFD) computations (Boundary Element Method for instance, as in Faye et al. (2024). FSI simulations can be used to optimize the performance of a hydrofoil by varying its geometric and structural properties (e.g. chord, thickness, fiber orientations, etc.), as shown in Temtching Temou (2020) and Sacher et al. (2018).

This paper validates a beam finite element model to study composite hydrofoils. The method validated in this paper is used in Faye et al. (2024) to develop a FSI coupling modelling flexible hydrofoils in a flume tank. Composite hydrofoils are characterized by anisotropic mechanical properties, which have to be considered in the Finite Element Analysis (FEA) to correctly capture the nonlinear structural phenomenons. Depending on the fiber orientation in the composite material, significant couplings between displacements and rotations may be present and impact the flow incidence seen by an hydrofoil submitted to an hydrodynamic loading (Temtching Temou, 2020). Nejatbakhsh et al. (2023) shows the influence of the BTC on the flutter speed and global stability of an airfoil.

In a FEA, composite hydrofoils are usually modeled with 3D solid and/or 2D shell finite elements (Temtching Temou, 2020; Mohammed Arab, 2020). In this paper, composite hydrofoils are modelled with 1D beam elements equivalent to the 3D model. To do so, the three-dimensional geometric nonlinear equilibrium analysis of the foil, considered as an elastic medium, is divided into a nonlinear one-dimensional analysis and a set of two-dimensional linear analysis of the cross sections (Hodges, 2006). To perform such an analysis, several software exist such as ANBA (Feil et al., 2020) or VABS (Yu et al., 2012) for the section analysis and GEBT (Yu and Blair, 2012) for the one-dimensional problem solving. In the present study, the tools implemented in Abaqus™ 2022 are used (Dassault Systèmes, 2022). No implementation is done in Abaqus™, the functionalities provided by Abaqus™ 2022 are recent and not yet validated to study hydrofoils. The objective of this paper is to test these recent features and validate the usage of the equivalent beam approach to study composite hydrofoils. In a preliminary study of a foil, its behavior in a flow can be studied with a Quasi-Static FSI simulation (Lothode et al., 2013), this is why the FEA method validated in this paper is static.

In this paper, static loads are applied on different foils and static structural responses are evaluated with a common 2D/3D FEA, an equivalent beam 1D FEA and an experimental setup. Then, the different results are compared to assess the validity of the equivalent beam model to study composite hydrofoils. The load cases in the numerical models are defined to match the experimental campaign. The paper is organized as follows. Section 2 presents the foils considered for the study and the proposed method to numerically model them with equivalent beam elements. Then, Section 3 introduces the experimental setup used to characterise the static structural responses of the foils. in Section 4, the setup of the numerical models reproducing the experiments is detailed. The Section 4 also highlights the reduction of the computational time made possible by the equivalent beam model. The numerical and experimental results are presented and discussed in Section 5. This Section 5 validates the equivalent beam model for the study of composite hydrofoils. In this Section 5, the stresses computed during the 2D/3D FEA and the 1D FEA are compared, to check if the equivalent beam model is able to estimate the maximum stress in a deformed foil.

2 METHOD FOR DETERMINING THE EQUIVALENT PROPERTIES OF A COMPOSITE HYDROFOIL

The modeling of a foil as an equivalent beam is considered as it is a slender structure comparable to a beam. It should be noted that the present study is limited to straight foils without initial twist and/or curvature.

2.1 Considered Foils

To assess and illustrate the method presented in this paper, the structural behavior of 4 foils having the same geometries but different fiber orientations is investigated. These 4 foils are shown in Figure 1. The foils have been manufactured with the same mold, they are straight and prismatic, and their geometry is a NACA0015 section (chord of 25 cm) extruded over 1.375 m. The dimensions of the foils are detailed in Table 2. The cross-sections of the foils, illustrated in Figure 2, are sandwich structures, constituted of an Airex web foam wrapped in a ply of glass-epoxy taffeta and a unidirectional (UD) glass-epoxy ply.

The frame $(\boldsymbol{E_1}, \boldsymbol{E_2}, \boldsymbol{E_3})$ is also represented in Figure 2. In this frame, the flexural deformation around $\boldsymbol{E_2}$ (principal direction of deformation in the experimental campaign) is denoted κ_2 and is positive when the foil is bent downwards. The torsion took by the foil is denoted κ_1 and is positive when the leading edge of the foil goes up. The signs of κ_1 and κ_2 are illustrated in Figure 2.

The only isotropic material is the Airex web, with properties detailed in Table 3. Orthotropic and transverse isotropic behaviors are respectively assumed for the taffeta and UD ply. The properties of these plies are given in Table 4, where 1 and 2 directions are respectively parallel to the warp and weft.

Among the 4 foils, only the UD orientation changes, where tested orientations are -10°, -30°, -30° and -50°. The fiber orientations are illustrated in Figure 1 with color mark lines, where the fibers are oriented such as the extrados of a foil is symmetric to its intrados. (Turnock et al., 2023) show that this symmetric configuration allows the apparition of a significant BTC.

The different orientations result in different stiffnesses (e.g. flexural, torsional, etc.) and different coupling intensities (e.g. BTC, extension-torsion coupling, etc.). The expected structural behaviors of the foils are gathered in Table 5. A similar study has been conducted through the work of Vanilla et al., 2021. The main difference with the present work is the method used to determine the equivalent properties of a composite structure. Indeed, the BTC intensity of the beam is extracted from experimental data in the work of Vanilla et al., 2021, whereas in the present work, it is computed with a section analysis algorithm, detailed in the following Section 2.2.

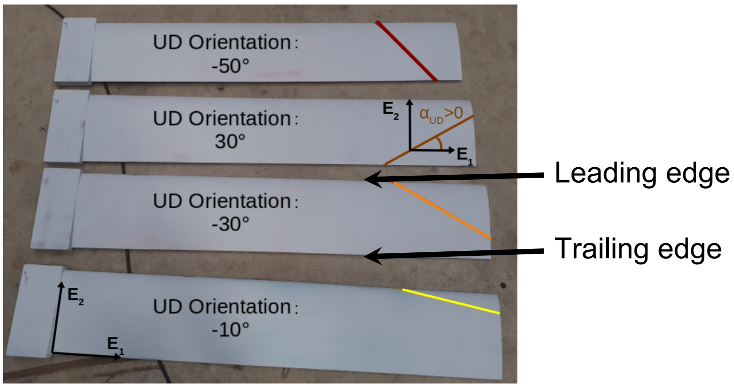

Figure 1. Tested hydrofoils.

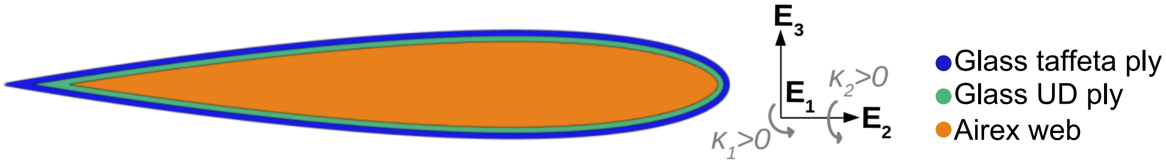

Figure 2. Cross section of the foils.

Table 2. Geometric properties of the foils.

Chord [m]	Span [m]	Taffeta ply thickness [mm]	UD ply thickness [mm]
0.250	1.375	9.45E-02	3.27E-01

Table 3. Mechanical properties of the Airex web.

Material	E [MPa]	ν [-]	ρ [kg/m^3]
Airex Foam	25.0	0.400	60

Table 4. Engineering constants of the materials constituting the skin of the foils.

Material	E_1 [GPa]	E_2 [GPa]	ν_{12} [-]	G_{12} [GPa]	G_{13} [GPa]	G_{23} [GPa]	ρ [kg/m^3]
Taffeta	16.0	16.5	0.108	1.81	0.9	0.9	1625
UD	27.4	5.1	0.348	1.81	1.81	0.9	1625

Table 5. Expected structural behaviors of the 4 foils.

UD ply orientation	Expected stiffness	Expected BTC intensity
-10°	high	low
-50°	low	medium
-30°	medium	high
30°	medium	high

2.2 Modeling of a Foil with 1D Equivalent Beam Elements

To model a foil with equivalent beam elements, the 3D problem is splitted into a combination of 2D linear sectional analyses and a 1D nonlinear finite element analysis. Thus, the structural behavior of a foil is predicted following the procedure outlined below :

- Determination of the equivalent properties of the cross-sections (2D problems);
- Predict the deformation of the foil with equivalent beam finite elements (1D problem);
- Reconstruction of 3D displacements and stresses from the results obtained with the equivalent beam model.

For this theory to be applicable, the studied foil has to be long and slender. It is also important to have smooth variations of the cross-sections' geometry and structural properties along the span. The methodology for evaluating the equivalent properties of an anisotropic and heterogeneous composite section (first step) is discussed below.

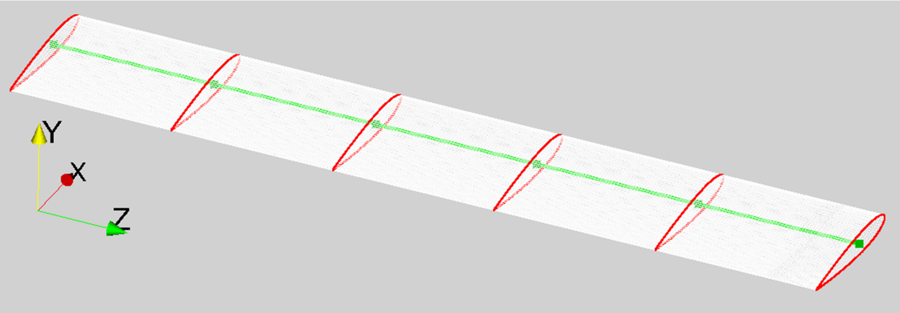

Figure 3. Illustration of the studied foil with six cuts.

To begin with, a 3D geometry is defined then partitioned into distinct regions corresponding to each material (UD, taffeta, and Airex in this study). This geometry is then segmented into multiple cross sections along its span, as illustrated in Figure 3. In the particular case of a prismatic hydrofoil, only one section analysis is performed because the properties of the cross-sections do not change along the span of the foil. The definition of a centerline is mandatory to model the foil with equivalent beam elements. As a first approximation, this line goes through the geometric centers of sections. This location is then corrected to have a centerline going through the shear centers of each section.

The shear center of a section is defined as the point where any load can be applied without inducing any twist. The computation of the shear center is done during the next step, which is the section analysis. During this step, a section is meshed and its elastic properties are integrated over its surface, to obtain a Timoshenko stiffness matrix $\boldsymbol{K}$ (see Eq. 1) representative of the equivalent properties of the considered section. The method used in Abaqus™ (Han and Bauchau, 2015) is complex and different from the one implemented in VABS (Yu et al., 2012). In VABS, the method uses an asymptotic development with respect to the axial deformation and the aspect ratio (AR) of the foil. The $\boldsymbol{K}$ matrix computed in VABS is associated to sectional strains relative to the rigid-body motion of the section. In Abaqus™, the section analysis is based on the stationarity of the Hamiltonian, considering the warping displacement and its associated dual impulse. The Green-Lagrange strains are considered to solve the problem. The $\boldsymbol{K}$ matrix computed with this method is associated to sectional strains relative to the rigid-body motion and warping of the section. A brief description of the method is given in the Section 2.3 of this paper.

Two section analyses are required, the first one to compute the shear center of the section (according to an arbitrary origin, the leading edge in the present study) and the second one to determine the equivalent properties at the shear center.

The Timoshenko stiffness matrix $\boldsymbol{K}$ computed during the section analysis relates the generalized internal forces F_i and moments M_i of the section to its generalized translational and rotational strains (also called curvature vector), respectively denoted γ_i and κ_i, such as:

$$\begin{pmatrix} F_1 \\ F_2 \\ F_3 \\ M_1 \\ M_2 \\ M_3 \end{pmatrix} = \begin{pmatrix} K_{11} & K_{12} & K_{13} & K_{14} & K_{15} & K_{16} \\ K_{12} & K_{22} & K_{23} & K_{24} & K_{25} & K_{26} \\ K_{13} & K_{23} & K_{33} & K_{34} & K_{35} & K_{36} \\ K_{14} & K_{24} & K_{34} & K_{44} & K_{45} & K_{46} \\ K_{15} & K_{25} & K_{35} & K_{45} & K_{55} & K_{56} \\ K_{16} & K_{26} & K_{36} & K_{46} & K_{56} & K_{66} \end{pmatrix} \begin{pmatrix} \gamma_1 \\ \gamma_2 \\ \gamma_3 \\ \kappa_1 \\ \kappa_2 \\ \kappa_3 \end{pmatrix}. \tag{1}$$

The $\boldsymbol{K}$ matrix developed in Eq. 1 is expressed in the frame $(\boldsymbol{E_1}, \boldsymbol{E_2}, \boldsymbol{E_3})$, illustrated in Figure 2. In this frame, the torsional and flexural strains of a foil submitted to a vertical concentrated load are respectively characterized by γ_1 and γ_2. The meanings of the diagonal terms of the section stiffness matrix are given below:

- K_{11} : Axial stiffness;
- K_{22} , K_{33} : Shear stiffness;
- K_{44} : Torsional stiffness;
- K_{55} , K_{66} : Flexural stiffnesses.

K_{45} and K_{46} terms quantify the intensity and the sign of the BTC. In the present case, only the term K_{45} is relevant because it is the one relating the torsion moment M_1 to the flexural strain κ_2. It also relates the flexural moment M_2 to the torsional strain κ_1 (see Eq. 1). More details on the interpretation of the BTC is given in Section 5.1, where the equivalent properties of the different foils are discussed.

There are other couplings in the material (e.g. extension-torsion coupling, extension-bending coupling, etc.), but the present work mainly focuses on the BTC because in most cases it has a higher influence than the other couplings when studying foils in FSI simulations. The shear center of the section can be computed from the terms of the compliance matrix S, as shown in (Hodges, 2006):

$$x^{cis} = -\frac{S_{34}^{cs}}{S_{44}^{cs}}; \quad y^{cis} = \frac{S_{24}^{cs}}{S_{44}^{cs}}. \tag{2}$$

A shear center computed with the Eq. 2 corresponds to the point of the section where the shear forces do not induce any twist. In the present case, the twist produced by the bend-twist coupling vanishes. After the determination of the shear center, a second section analysis is realized with the shear center as the origin, to evaluate the equivalent properties of the section according to the shear center.

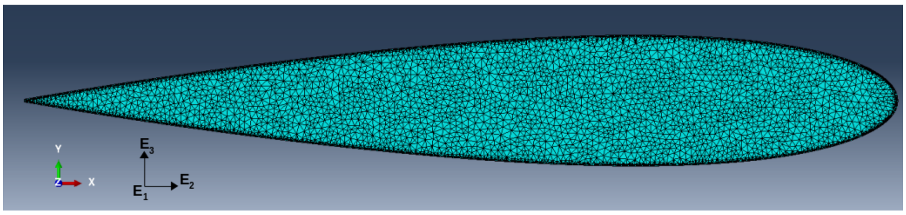

Figure 4. Triangular mesh of the cross section of a foil.

In Abaqus™, the cross sections are meshed with triangular elements WARPF2D3, which allows us to easily mesh complex geometry (trailing edge of the section for instance). A mesh sensitivity analysis is performed to determine the optimal mesh for which the values of the matrix $\boldsymbol{K}$ are converged. The associated mesh is illustrated in Figure 4. The section analysis also computes the mass properties and the warping functions of the sections. The warping functions are used to compute the Green strain and the Cauchy stress tensors in a section of an equivalent beam element.

Once the section analysis is done, the next step is the reconstruction of 1D finite beam elements from the section stiffness matrices. The reconstructed beam elements must be able to model the couplings in the material. To do so, the section matrix can be integrated along the length of the beam element, as explained in (Stäblein and Hansen, 2016). In the present work, Abaqus™ 2022 is used to construct the equivalent beam as an assembly of beam elements. For each beam element, a stiffness matrix $\boldsymbol{K_b}$ is computed from the cross-section stiffness matrix $\boldsymbol{K}$ and the strain- displacement matrix $\boldsymbol{B_b}$ of a beam element. Then, a global stiffness matrix $\boldsymbol{K_g}$ is assembled from the contribution of each beam element stiffness matrix. $\boldsymbol{K_g}$ is a tensor of dimension $[6(N_b+1)] \times [6(N_b+1)]$, where N_b is the number of beam elements considered to discretize the foil, and expressed as :

$$\boldsymbol{K}_g = \sum_{b=1}^{N_b} \int_{L_b} \boldsymbol{B}_b^T \boldsymbol{K} \boldsymbol{B}_b dz. \tag{3}$$

In Eq. 3, L_b represents the length of a given beam element. $\boldsymbol{B_b}$ depends on the choice of the beam element in Abaqus™ because it is constructed from the shape functions of the beam element. In Abaqus™ 2022, the only beam element considering the cross-section stiffness matrix $\boldsymbol{K}$ as an input is the element B31, a linear Timoshenko beam element with unconstrained warping. Therefore, in this paper, all the numerical results associated with the equivalent beam approach are obtained with B31 elements. Once the global stiffness matrix $\boldsymbol{K_g}$ is computed, the boundary conditions and loads are defined, and a FEA is performed. Following the FEA, translation and rotation vectors are obtained for each node, leading to the equivalent beam deformations. Section stresses and strains are also computed for each element. The deformed 3D geometry is extrapolated from the nodal displacements and rotations with the linear shape functions of a Timoshenko beam element. The shape functions are chosen according to the type of beam element used in the FEA. To reconstruct a 3D deformed geometry (considered as a point cloud), each of its points is projected on the closest beam element:

- The 3D point is projected on a node of a beam element → its displacement is computed from the associated nodal displacement, nodal rotation and warping functions of the section;

- The 3D point is projected on an arbitrary point of a beam element → nodal displacement and rotation are computed from the displacements and rotations of the nodes and the linear shape functions → the displacement of the 3D point is computed accordingly.

The linear shape functions of a Timoshenko beam element (Oñate, 2013) are presented below in Eq. 4, where u_i is the translation along the axis i and θ_i is the rotation around the axis i. Thus, the index i can be x, y or z.

$$u_i = N_1 u_i^1 + N_2 u_i^2; \quad \theta_i = N_1 \theta_i^1 + N_2 \theta_i^2 \tag{4}$$

Eq. 4 relates the displacement and rotation of an arbitrary point of a beam element with the displacements and rotations of its two nodes. The position of an arbitrary point belonging to a beam element is described by a local adimensional variable ξ varying between 0 and 1. The shape functions N_1 and N_2 depend on this variable and are given below:

$$N_1(\xi) = 1 - \xi; \quad N_2(\xi) = \xi. \tag{5}$$

Because the sections of a foil are perpendicular to its centerline, the displacements of the points of a section are all projected on the same beam element and thus, their displacements are computed from the same nodal displacement (which can be the result of an interpolation of two nodal displacements). Thus, the motion of the sections is assumed to be rigid during the reconstruction of the 3D deformed foil. To consider the deformation of the sections in the reconstruction of the 3D geometry, the warping displacement of a section can be computed in Abaqus™ 2022 from the warping functions and the deformed beam elements. If the warping displacement of the sections is not computed during the 3D reconstruction, the sections of the foil have a rigid body motion. Abaqus™ also computes the Green strain and the Cauchy stress tensor in the section, which are useful to conclude on the structural integrity of the foil under a given loading.

2.3 Section Analysis Algorithm

The section analysis method used in this paper is the one implemented in Abaqus™, proposed by Han and Bauchau, 2015 and based on the work of Giavotto et al., 1983. The methods lead to identical results and their major difference is the starting point used to determine the governing equations of the problem. In (Han and Bauchau, 2015), they are derived from the canonical approach of Hamilton, whereas in Giavotto et al., 1983, it is derived from the principle of virtual work. For simplicity, the theory of the cross-section analysis is presented using a notation close to the one of Giavotto et al., 1983. Every symbol written is bold is assumed to be a tensor and the coordinate system is presented in Figure 4.

Firstly, the displacement of a point of the cross section $\boldsymbol{v}$ is decomposed into a rigid body motion $\boldsymbol{w}$ and a warping displacement $\boldsymbol{g}$. The rigid motion is then expressed from the three components of the rigid translation $\boldsymbol{\chi}$ and rotation $\boldsymbol{\phi}$ of the cross section (for a given reference point). The warping displacements at a given point can be expressed from the shape functions $\boldsymbol{N}$ of the elements used to mesh the section and its nodal displacements $\boldsymbol{u}$ (i.e warping displacements). Thus, the displacement of a point of the cross section can be written as:

$$\boldsymbol{v}(x, y) = \boldsymbol{w} + \boldsymbol{g} = \boldsymbol{Z}(x, y)\boldsymbol{r} + \boldsymbol{N}(x, y)\boldsymbol{u}, \tag{6}$$

where $\boldsymbol{Z}$ and $\boldsymbol{r}$ are defined as:

$$\boldsymbol{Z}(x,y) = \begin{pmatrix} 1 & 0 & 0 & 0 & 0 & -y \\ 0 & 1 & 0 & 0 & 0 & x \\ 0 & 0 & 1 & y & -x & 0 \end{pmatrix}, \tag{7}$$

and

$$\boldsymbol{r} = [\chi_x; \chi_y; \chi_z; \phi_x; \phi_y; \phi_z]^T. \tag{8}$$

The deformations of the cross section are associated to a strain-curvature vector $\boldsymbol{\Psi}$, containing the generalized strain and curvature measures, respectively denoted γ and $\boldsymbol{\kappa}$ and defined as:

$$\boldsymbol{\Psi} = [\gamma_x; \gamma_y; \gamma_z; \kappa_x; \kappa_y; \kappa_z]^T, \tag{9}$$

$$\gamma_x = \frac{\partial \chi_x}{\partial z} - \phi_y; \gamma_y = \frac{\partial \chi_y}{\partial z} + \phi_x; \gamma_z = \frac{\partial \chi_z}{z}, \tag{10}$$

$$\kappa_x = \frac{\partial \phi_x}{\partial z}; \kappa_y = \frac{\partial \phi_y}{\partial z}; \kappa_z = \frac{\partial \phi_z}{\partial z}. \tag{11}$$

The details of the terms of the curvature and strain of the section comes from the classical beam theory. Such results can be found in Andersen and Nielsen (2023). For convenience, the equation above can be written in its matrix form:

$$\boldsymbol{\Psi} = (\boldsymbol{T}_r + \frac{\partial}{\partial z})\boldsymbol{r}; \quad \boldsymbol{T}_r = \begin{pmatrix} 0 & 0 & 0 & 0 & -1 & 0 \\ 0 & 0 & 0 & 1 & 0 & 0 \\ 0 & 0 & 0 & 0 & 0 & 0 \\ 0 & 0 & 0 & 0 & 0 & 0 \\ 0 & 0 & 0 & 0 & 0 & 0 \\ 0 & 0 & 0 & 0 & 0 & 0 \end{pmatrix}. \tag{12}$$

From the expression of the displacement of an arbitrary point of the cross-section, the strain, considered small, can be written such as:

$$\epsilon_{ij} = \frac{1}{2}(\frac{\partial v_i}{\partial j} + \frac{\partial v_j}{\partial i}). \tag{13}$$

The strains and stresses vectors in the section, respectively denoted $\boldsymbol{\epsilon}$ and $\boldsymbol{\sigma}$ are expressed using the Voigt notation, meaning that:

$$\boldsymbol{\epsilon} = [\epsilon_{xx}; \epsilon_{yy}; 2\epsilon_{xy}; 2\epsilon_{xz}; 2\epsilon_{yz}; \epsilon_{zz}]^T, \tag{14}$$

$$\boldsymbol{\sigma} = [\sigma_{xx}; \sigma_{yy}; \sigma_{xy}; \sigma_{xz}; \sigma_{yz}; \sigma_{zz}]^T. \tag{15}$$

These two vectors are related by Hooke's law $\boldsymbol{\sigma} = \boldsymbol{Q}\boldsymbol{\epsilon}$, where $\boldsymbol{Q}$ is the material constitutive matrix. Before writing the governing equations of the problem, the displacements of the nodes constituting the section have to be constrained. The warping displacements expressed in Eq. 6 are coupled to the rigid motion of the sections, meaning that the warping contributes to the rigid body motion, which is not physical. To correct this, the following set of constraints for the displacements and their derivatives is defined:

$$\begin{pmatrix} \boldsymbol{D}^T & \boldsymbol{0} \\ \boldsymbol{0} & \boldsymbol{D}^T \end{pmatrix} \begin{pmatrix} \boldsymbol{u} \\ \frac{\partial \boldsymbol{u}}{\partial z} \end{pmatrix} = \begin{pmatrix} \boldsymbol{0} \\ \boldsymbol{0} \end{pmatrix}. \tag{16}$$

$\boldsymbol{D}$ is defined below, with n corresponding to the number of nodes in the mesh of the cross-section:

$$D = \begin{pmatrix} 1 & 0 & 0 & ... & 1 & 0 & 0 \\ 0 & 1 & 0 & ... & 0 & 1 & 0 \\ 0 & 0 & 1 & ... & 0 & 0 & 1 \\ 0 & 0 & y_1 & ... & 0 & 0 & y_n \\ 0 & 0 & -x_1 & ... & 0 & 0 & -x_n \\ -y_1 & x_1 & 0 & ... & -y_n & x_n & 0 \end{pmatrix}^T. \tag{17}$$

To determine the governing equations of the problem, the internal forces $\boldsymbol{\theta}$ are defined, such as $\boldsymbol{\theta} = [T_x; T_y; T_z;\ M_x; M_y; M_z]^T$, where T_i and M_i respectively represent the internal forces and moments. For instance, in the present coordinate system, T_z represents the axial internal force in the section. It is shown in Giavotto et al. (1983) that the expression of the derivative of $\boldsymbol{\theta}$ can be computed as:

$$\frac{\partial \boldsymbol{\theta}}{\partial z} = \boldsymbol{T}_r^T \boldsymbol{\theta}. \tag{18}$$

Han and Bauchau (2015) shows that, using Hamilton's canonical approach, the section stiffness matrix can be computed by taking into account the warping effects in the section. The resulting matrix is a Timoshenko matrix relating the forces applied on the section to its strains (see Eq. 1). The meaning of the terms of this matrix is discussed in Section 5.1.

3 EXPERIMENTAL SETUP

In this Section 3, the experimental setup used to characterize the static displacements of the foils for several load cases is detailed. The experimental setup is illustrated in Figure 5 and Figure 6, where a foil is cantilevered, and masses are suspended to it at several locations. To have the best clamping possible, the foils have a parallelepiped heel (see Figure 5) which is rigidly linked to a support into an aluminum block. To avoid any motion of the foil, the aluminum block has screws which are tightened with a torque wrench to reproduce the same clamping condition for each foil. A clamping beam is used to suspend the masses to the foil (see Figures 5 and 7), this allows the application of eccentric forces on the foil and thus induces a significant torsion that is then compared with the numerical results. The clamping beam is 1 m long, 10 cm tall and 4 cm wide.

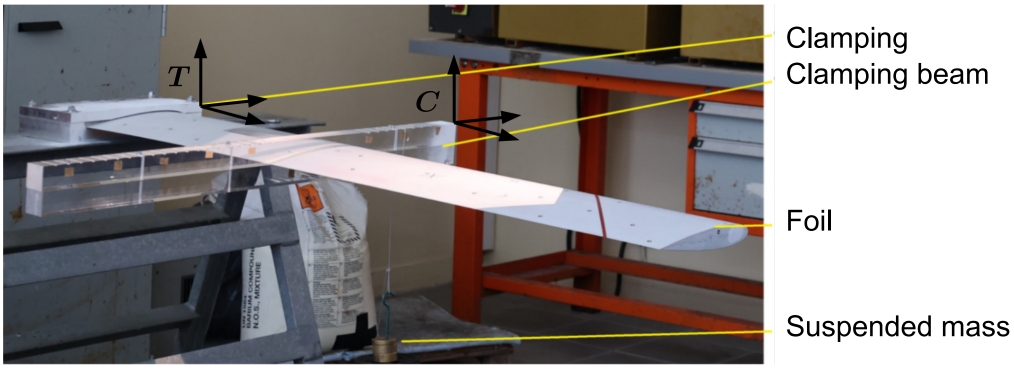

Figure 5. Experimental device used to study the mechanical properties of the foils.

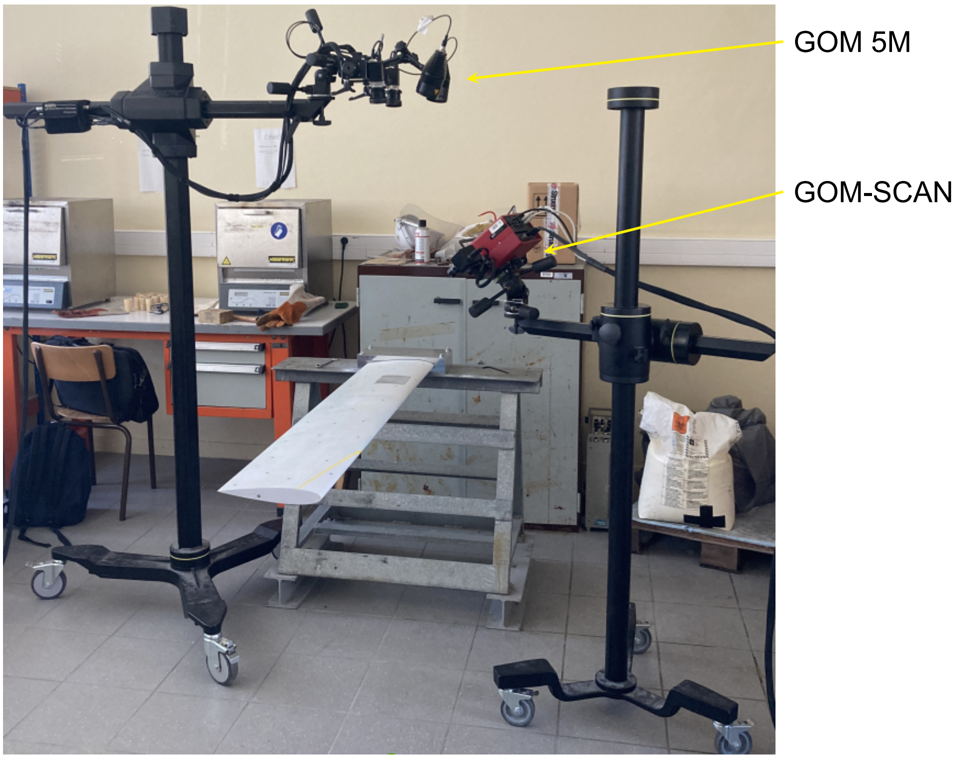

Figure 6. Cameras used to capture the shape of the upper surface of the foils.

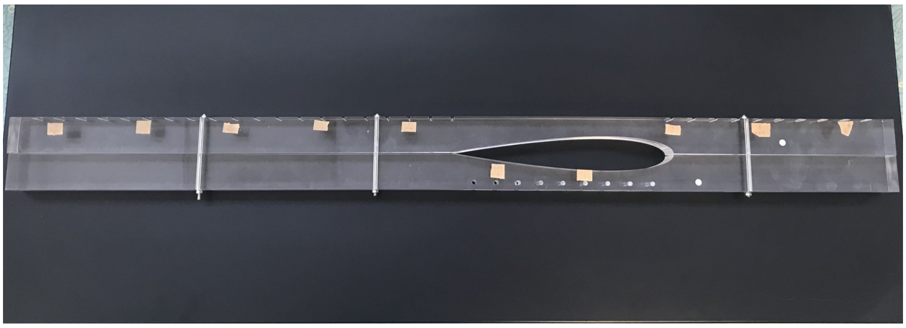

Figure 7. Clamping beam used to suspend the masses to the foil.

In Figure 6, no loads are applied and there are two recording devices which are used to compute the local and the global displacements of the foils. The local displacements are recorded with the GOM 5M system (on the left in Figure 6) and the global displacements are measured with the GOM-SCAN system (on the right in Figure 6). The measurement principles are detailed in the following of the present Section 3.

3.1 Global Displacement

In this Section 3.1, the measurement method associated with the GOM-SCAN is presented. The GOM-SCAN is a mobile scanner able to acquire the shapes of the foils for different loading cases. To acquire the shape of a foil, the GOM-SCAN system projects light fringes on its upper surface and with its cameras, it is able to determine the shape of the surface from the fringe deformations. A preliminary calibration of the scan is made before the measurements. Because this scanner is mobile, it requires landmarks that are located all along the upper surface of the foils. With at least 3 visible points per scan, the GOM-SCAN is able to reconstruct the upper surface of a foil within 10 to 20 acquisitions at different locations. The corner of the clamping beam is also acquired by the scan (in white in Figure 5). Its displacement and rotation with respect to the clamping are recorded for each load case and compared with the results obtained numerically. The displacements are measured according to a reference configuration where the clamping beam is installed on the foil but no loads are suspended to it. Thus, the foils are submitted to their own weights and the weight of the clamping beam, which is about 3.54 kg. This reference configuration is chosen to reduce the uncertainties on the measurement associated with the installation of the clamping beam.

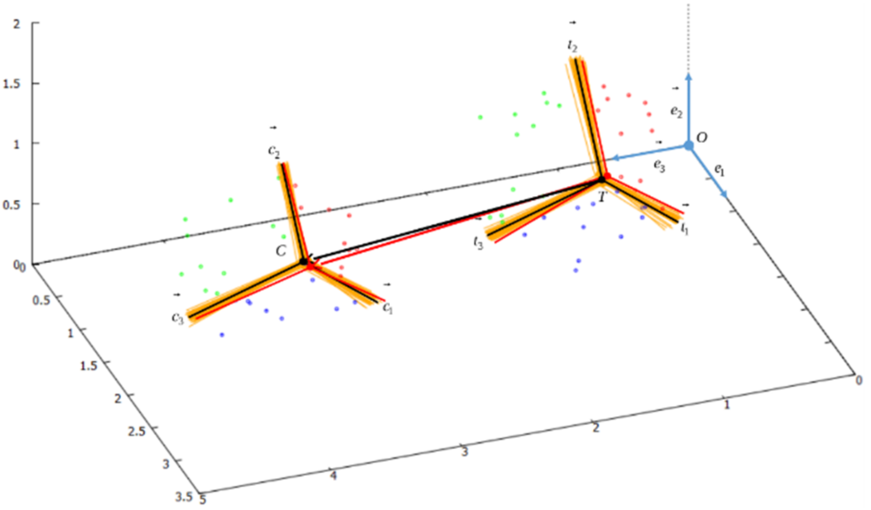

Figure 8. Illustration of the uncertainties estimation for $n_t = 33$, $n_p = 6$ and $\epsilon_t = \epsilon_c = 2.0E-02$.

For a given foil and a given loading case, the GOMSCAN returns the deformed shape of the upper surface of the foil and the deformed position of the corner of the clamping beam. For its measurements,the GOM-SCAN constructs an arbitrary coordinate system which does not match the one of the numerical computations. To compute the displacements from these results in the numerical reference frame (see Figure 5), a program is used to construct two frames, a first one at the clamping and a second one at the corner of the clamping beam corner. Knowing the position and the orientation differences between the two frames, the displacement and rotation of the corner of the clamping beam is deduced. Because the clamping device and the corner of the clamping beam are not perfectly parallelepiped, there are significant uncertainties on the computed values. The uncertainties on the frame acquisitions are illustrated in Figure 8.

ϵ_t and ϵ_c are the amplitudes of Gaussian noises used to simulate the error associated with the manual acquisition of the frames. The half amplitude of the Gaussian noise represents the ratio between the precision of the measure and a characteristic length of the area where the measure is carried out (around 20 cm in the present study). To evaluate the uncertainties, two analytical frames are defined, corresponding to the two corners of reference. The two frames are characterized by an origin and an orientation. The corner of the clamping and the corner of the clamping beam are respectively defined as ($\boldsymbol{T}$,$\boldsymbol{t_i}$) and ($\boldsymbol{C}$,$\boldsymbol{c_i}$) where i represents the three directions in space (i.e. i = 1, 2, 3). For each plane of each frame, a number n_p of points is generated with a centered Gaussian noise for the out-of-plane component. Because the corner of the clamping beam is more parallelepiped than the corner of the clamping device, the corner of the clamping beam is easier to capture and thus, it is characterized by a smaller Gaussian noise. The determination of the noise amplitude is discussed later in this section. The Gaussian noises considered at the clamping and the clamping beam are respectively denoted ϵ_c and ϵ_t . After the generation of the noisy points, for each frame, there are $3n_p$ imperfect points from which an approximated frame can be computed with a least square regression. Then, with the theoretical frame, a difference is computed for the origin of the estimated frame and its orientation. This protocol is repeated n_t times to simulate a great number of acquisitions and determine the mean error for a measurement. In Figure 8, the frames of reference are illustrated in black. In this same Figure 8, 33 frames are generated, and the imperfect points (in green, blue and red) are shown for the first and the last iteration. The 33 generated frames are represented in orange and the k^{th} frame is represented in red. To clearly illustrate the method in Figure 8, a noise of $2E-02$ is considered for ϵ_c and ϵ_t .

For each iteration k and each direction in space, the uncertainties on the position δx_i^k and rotation δr_i^k of the point $\boldsymbol{C}$ with respect to the point $\boldsymbol{T}$ (see Figure 8) are computed. The formulas used to compute the uncertainties are given below, where $i = 1, 2, 3$:

$$\frac{\delta x_i^k}{L_{ref}} = -\frac{\boldsymbol{T^k C^k} \cdot \boldsymbol{t_i^k} - \boldsymbol{TC} \cdot \boldsymbol{t_i}}{\|\boldsymbol{TC}\|}, \tag{19}$$

$$\begin{aligned} \delta r_1^k = \frac{90}{\pi} \Big(& \arccos\left(\left(\boldsymbol{c_2^k} - \left(\boldsymbol{c_2^k} \cdot \boldsymbol{c_1^k}\right) \boldsymbol{c_1^k}\right) \boldsymbol{t_2^k}\right) + \arccos\left(\left(\boldsymbol{c_3^k} - \left(\boldsymbol{c_3^k} \cdot \boldsymbol{c_1^k}\right) \boldsymbol{c_1^k}\right) \boldsymbol{t_3^k}\right) \\ & - \arccos\left(\left(\boldsymbol{c_2} - \left(\boldsymbol{c_2} \cdot \boldsymbol{c_1}\right) \boldsymbol{c_1}\right) \boldsymbol{t_2}\right) - \arccos\left(\left(\boldsymbol{c_3} - \left(\boldsymbol{c_3} \cdot \boldsymbol{c_1}\right) \boldsymbol{c_1}\right) \boldsymbol{t_3}\right)\Big) . \end{aligned} \tag{20}$$

The expression of δr_2^k and δr_3^k can be retrieved by performing a circular permutation of the Eq. 20. After the n_t iterations, the mean uncertainties for each displacement and rotation component are computed, such as:

$$\left.\frac{\delta x_i}{L_{ref}}\right|_{\text{mean}} = \frac{\text{mean}\left(\delta x_i^k\right)}{L_{ref}} \quad ; \quad \left.\frac{\delta x_i}{L_{ref}}\right|_{\text{std}} = \frac{\text{std}\left(\delta x_i^k\right)}{L_{ref}}, \tag{21}$$

$$\delta r_i|_{\text{mean}} = \text{mean}\left(\delta r_i^k\right) \quad ; \quad \delta r_i|_{\text{std}} = \text{std}\left(\delta r_i^k\right). \tag{22}$$

Finally, the relative uncertainty on the displacement and the absolute uncertainty on the rotation are computed with:

$$\frac{\delta x}{L_{ref}} = \max\left(\left.\frac{\delta x_i}{L_{ref}}\right|_{\text{mean}} \pm 2 \left.\frac{\delta x_i}{L_{ref}}\right|_{\text{std}} \right), \tag{23}$$

$$\delta r = \max\left(\delta r_i|_{\text{mean}} \pm 2\, \delta r_i|_{\text{std}}\right). \tag{24}$$

During the post-processing of the results, the points belonging to the faces of each corner are selected by hand, the optimal value found for n_p is 6. It corresponds to the minimal number of points per face needed to find a consistent frame for a given corner.This post-processing method is one of the sources of uncertainty. The half amplitude of the Gaussian noise represents the ratio between the precision of the measure and a characteristic length of the area where the measure is carried out (around 20 cm in the present study). To compute the displacement of the foil, two acquisitions of its shape must be performed. In the first one, the foil is scanned in its reference configuration (i.e. clamping beam without mass suspended to it), this scan is only done once for each foil. Then, for every load case, the shapes of the loaded foils are acquired, and their displacements are computed according to the reference configuration. To compute the Gaussian noise ϵ_c associated with the clamping beam, a reference length of 5 cm is considered and the precision of the measure is about 0.01 mm. At the clamping, the reference length of the measure is 20 cm and its precision is 0.2 mm. Thus, the value for ϵ_c is $2E-04$ and the value of ϵ_t is $1E-03$. The precision of the measure is lower at the clamping because of machining planarity errors, which are higher at the clamping. Table 6 gives the estimated uncertainties computed for a single acquisition.

Table 6. Estimated uncertainties for a single acquisition of a displacement with the GOM-SCAN.

ϵ_c	ϵ_t	$\frac{\delta x}{L_{ref}}$	$\delta r[°]$
2.00×10^{-4}	1.00×10^{-3}	2.01×10^{-3}	1.68×10^{-1}

Because the shape of a foil is acquired twice, the uncertainties on the results are the double of the values presented in Table 6. In the present case, the absolute uncertainty on the rotation is about 0.336° and the relative uncertainty on the displacements is about $4E-03$.

3.2 Local Displacement

In this Section, the GOM 5M, which computes a local displacement field in a small area, is presented. In the present case, the area scanned by the GOM 5M is a rectangle with the dimension 100 × 120 mm located on the upper surface of the foils.

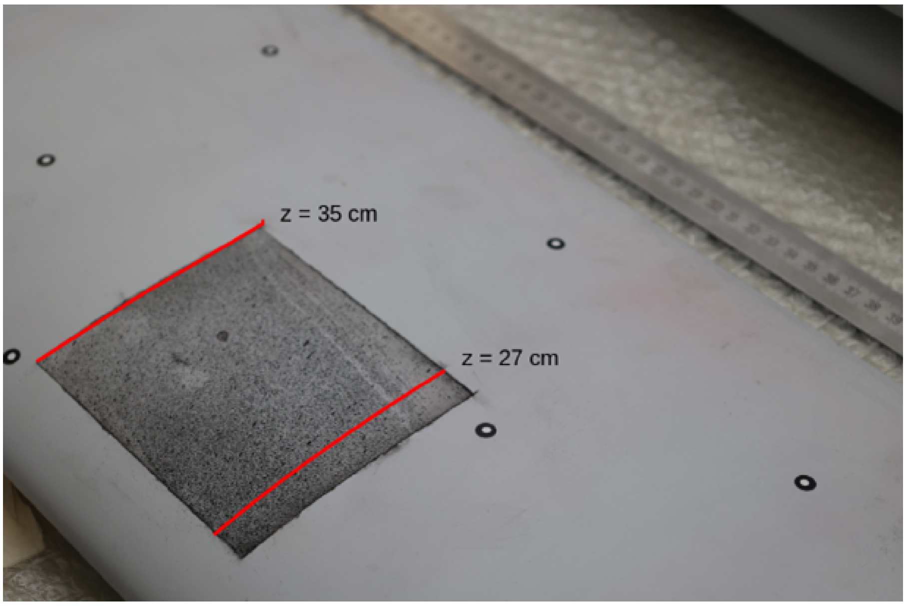

Figure 9. Speckle used by the GOM 5M to compute deformations.

The measurement area for the GOM 5M is chosen to maximize the computed strains. For a cantilevered foil, the maximum strain occurs near the clamping. The GOM 5M acquisition area is therefore located between $Z = 0.25$ m and $Z = 0.35$ m, where measured displacements are maximized without encountering any acquisition problems due to the clamping. In the acquisition area, a random speckle (see Figure 9) is generated to create markers for the GOM 5M. Then, with Digital Image Correlation (DIC, see (Jorge et al., 2022)), the GOM 5M computes a displacement field from an acquisition of the speckle in a reference configuration and an acquisition in the deformed configuration. To characterize a mean strain of the foil near the clamping, the difference between the displacements along the span of the extremities of the speckle (see $Z = 0.27$ m and $Z = 0.35$ m in Figure 9) is computed.To reduce the uncertainties, the displacement field is computed as the average of 6 acquisitions. As in Section 3.1, the reference configuration considered is the foil with the clamping beam installed but without mass suspended to it. This suppresses the potential errors caused by the installation of the clamping beam on the foil. After the measure, the GOM 5M returns a cloud point with a value of displacement along the span at each point. The displacement of a point is computed from a DIC performed on a rectangle of 11 per 19 pixels. Therefore, the values of displacement are averaged around their zone of interest and the uncertainty of the value is defined as the standard deviation of the displacement in the zone of interest.

4 FINITE ELEMENT MODEL OF THE FOILS

In this Section 4, the two finite element models used to capture the deformation of a foil for a given load case are presented. The load cases and boundary conditions in the finite element models are chosen to match as much as possible the experimental load cases (presented in Section 3). The method to evaluate the displacement of the foil is also derived from the experimental protocol.

In the experimental campaign, illustrated in Figure 5, the foils are cantilevered and their structural responses are evaluated for several concentrated load cases. A clamping beam is used to suspend a mass to the foil, this allows the application of eccentric forces on the foil and thus induces a significant torsion that is then compared with the numerical results. The experimental values of displacement of the foil are measured at the white corner of the clamping beam (see Figure 5) and they are measured relatively to a reference configuration where the clamping beam is installed but no masses are suspended to it.

4.1 Finite Element Model 3D

In this paper, the 2D/3D finite element model is referred to as *Abaqus 3D*. In the 2D/3D FEA, the foil is decomposed in two parts, a first one containing the Airex foam web, meshed with 3D solid elements. The second part is meshed with 2D shell elements and represents the skin of the foil (taffeta and UD). The 2D shell elements used for the skin drastically reduce the size of the structural mesh because the skin is not discretized along its thickness. The 3D solid elements used to model the web are 8 node brick elements C3D8R. A mesh sensitivity analysis has been performed to provide the optimal number of elements to correctly capture the behavior of the foils. The meshed web, illustrated in Figure 10, is made of 700 000 elements. The optimal mesh for the skin is constituted of 60 000 elements (see Figure 10). The 2D elements used for the skin are triangular Kirchhoff shell elements STRI3. On these elements, a composite layup is defined to specify the thickness of the layers and the fiber orientations. A Tie constraint is also defined to link the skin to the web. This constraint imposes the surface of the web to have the same motion as the 2D skin of the foil.

To match the experimental loading case in Abaqus™, the skin of the foil is partitioned to represent the contact surface between the clamping beam and the skin (see Figures 5 and 7). Then, with a multi-point constraint (MPC), this surface is constrained to follow a reference point as a rigid body (*loadingPoint* in Figure 11) and a concentrated load corresponding to the suspended mass is applied on this reference point. To model the clamping of the heel, the displacement of the skin and the web are constrained to be null in $Z = 0$ m. This is illustrated in Figure 11 with the blue and orange arrows. In Figure 11, the partition corresponding to the clamping beam is located at X = 0.8 m. There are two more reference points in the model, corresponding to the center of gravity of the clamping beam and its corner. These points are rigidly linked to the *loadingPoint* with a MPC and are respectively used to take into account the weight of the clamping beam (3.54 kg) and to measure the displacement and rotation of the corner of the clamping beam. The displacement is recorded at this particular point to be compared with measurements. A gravity load is also defined ($\boldsymbol{g} = -9.81\boldsymbol{y}m/s^2$, where $\boldsymbol{y}$ is defined in Figure 11) to consider the weight of the foil.

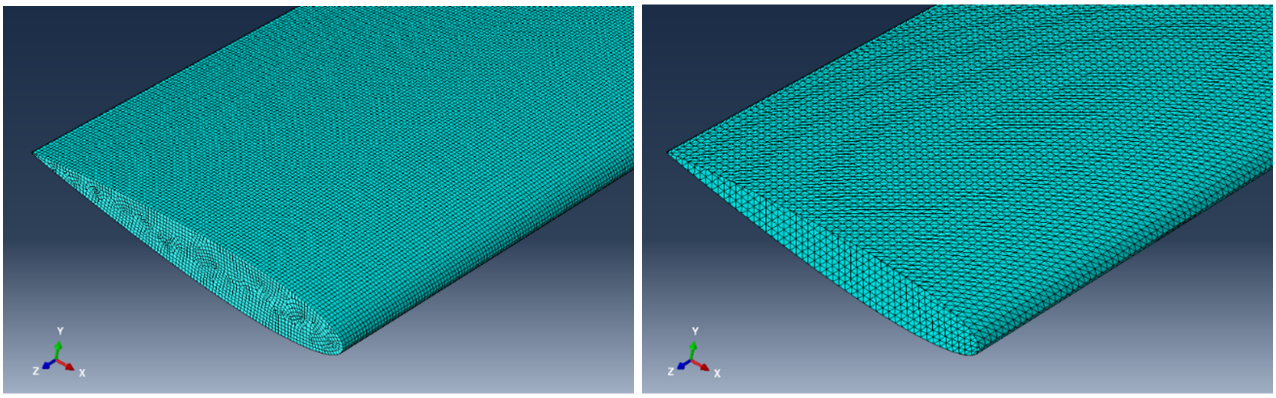

Figure 10. Finite element mesh of the web (left) and the skin (right) of the foils.

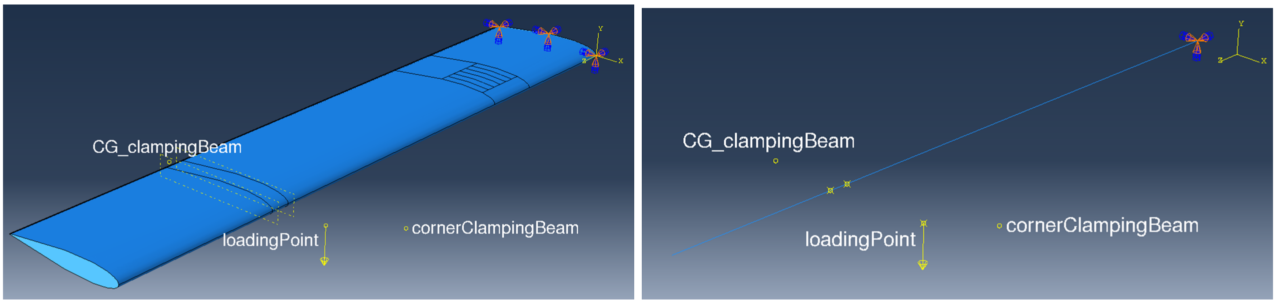

Figure 11. Illustration of the loading case and boundary conditions in Abaqus™ for the 3D model (left) and the equivalent beam model (right).

The skin of the foil is also partitioned near the clamping to easily extract local displacements between $Z = 0.27$ m and $Z = 0.35$ m. Such results are compared with experimental results given by the GOM-5M in Section 5.4.

Finally, the nonlinear FEA is solved with a specific Quasi-Static (QS) resolution based on a dynamic Euler Scheme (Hairer et al., 2008), as presented in the work of Sacher et al., 2020. This scheme is used because its natural damping helps the convergence towards a nonlinear static equilibrium. To set up the model in Abaqus™, a QS Dynamic Implicit Step is defined where the total computation time T_{end} , the initial time step T_0 and the minimal time step value T_{min} have to be defined. To compute these values, an initial modal analysis is performed to extract the first eigenfrequency of the foil f_1 . Then, the specific times are computed such as:

$$T_{end} = \frac{3}{f_1} \quad ; \quad T_0 = \frac{0.05}{f_1} \quad ; \quad T_{min} = T_0.10^{-4}. \tag{25}$$

Finally, to ensure the exact static convergence, a standard Newton-Raphson nonlinear static resolution is performed, meaning that the geometric nonlinearities are modelled.

4.2 Finite Element Model 1D

In the present study, the 1D finite element model is referred to as *Abaqus 1D*. In the 1D finite element model, a single section analysis is performed per foil because they are prismatic. The integration of the mechanical properties of a section is made with the mesh shown in Figure 4, which is composed of 12 000 elements. The optimal refinement of this mesh has been determined with a mesh sensitivity analysis. The elements used to mesh a section are triangular elements WARPF2D3, that capture the in-plane and out-of-plane warping of the sections. As explained in Section 2.2, the section analysis is realized at the shear center of the sections. The computed shear centers are functions of the UD orientation, and their computed values are presented in Table 7 for each foil. The coordinates of the shear centers are expressed in the frame presented in Figure 4. In this frame, the origin is located at the leading edge of the foil.

Table 7. Shear centers of the 4 foils sections.

UD Orientation	Shear Center (X, Y)
-50°	(-92.56, 0.00) mm
-30°	(-92.11, 0.00) mm
-10°	(-94.46, 0.00) mm
30°	(-92.11, 0.00) mm

The equivalent foil modelled in Abaqus™ is made of 70 beam elements, this number of elements was determined with a mesh sensitivity analysis. The beam elements used in the 1D finite element model are 2 nodes linear Timoshenko beam elements, denoted B31 in Abaqus™. The nodes of the beam elements go through the shear centers of the sections of the foil. The FEA is computed using a standard Newton-Raphson resolution, thus, modelling the geometric nonlinearities. A clamping condition is defined at the base of the foil ($Z = 0$m) and a concentrated load is applied as in the 3D finite element model. To do so, a reference point is defined (*loadingPoint* in Figure 11) to model the point where the mass is suspended. Then, with a MPC, the reference point is rigidly linked to the beam elements corresponding to the location of the clamping beam along the span of the foil (see yellow circles in the right part of Figure 11). The *loadingPoint* is also rigidly linked with a MPC to the reference points *CG_clampingBeam* and cornerClampingCarcan, which are respectively used to model the weight of the clamping beam and to easily record the displacement of the corner of the clamping beam. The loading case and the boundary condition are shown in Figure 11. Finally, to apply the gravity, a set of nodes going through the centers of mass of the section is created. These nodes are then rigidly linked with MPC to the nodes of the equivalent beam elements and a gravity load representative of the weight of the foil is applied on each of these nodes. The gravity is applied this way because the mass center of the section of a foil is different from its shear center.

4.3 Computational Time

The 1D FEA is considerably faster than the 3D FEA. This is mostly due to the number of elements which is 10 000 times higher in the 3D FEA. To illustrate the time saved when using the equivalent beam approach, different computational times for a FEA performed on the foil with the -50° UD orientation are provided in Table 8. The load case defined in this FEA is chosen to be representative of the load cases considered in this study. A mass of 5 kg is suspended from the foil at the location $(0.2, 0.0, 0.8)$ m, expressed in the frame defined in Figure 11.

Table 8. Computational cost of the FEA with the two methods for the -50° orientation.

	Processors number	Computational time [s]
Abaqus 3D	16	1.4E+05
Section analysis	1	6.1E+00
Abaqus 1D	1	1.0E-01
3D geometry reconstruction	1	1.2E-01
Warped section reconstruction	1	4.4E+01

The computational time associated with *Abaqus 1D* in Table 8 is split in 4 contributions, the section analysis, the 1D FEA, the reconstruction of the 3D geometry from the shape functions and finally the determination of the stress, displacements and deformation in the warped section. To reconstruct a 3D geometry while considering the warping of the sections, it is mandatory to reconstruct the warped sections at each beam node. Meaning that, in the present work, the *Warped section reconstruction* step is performed 71 (the number of beam elements considered is discussed in the previous Section 4.2. Thus, the time required to study the 3D deformation of the foil with beam elements considering the warping is about 50 minutes.

If the warping of the section is neglected, this time becomes 6.3 seconds. The 3D FEA is realized with 16 processors and despite that, the equivalent beam method is still faster, whether the warping is neglected or not. *Abaqus 1D* is 20 000 times faster than *Abaqus 3D* if the warping is neglected and it is 50 times faster when the warping is considered. The results illustrate the benefits of the equivalent beam method to save time in structural computations. The time saved by the equivalent beam method is even higher in FSI computations because the section analysis is only performed once at the beginning of the computation. For more complex foils with varying sections, the section analysis step would obviously require more computational time since in the present case, the section analysis is only done once.

5 RESULTS AND DISCUSSIONS

5.1 Section Stiffness Matrix

In this Section 5.1, the stiffness matrices obtained during the section analysis are discussed. Some terms of these matrices are then used to explain the structural behavior of the foils according to their UD orientation. Table 9 provides the significant terms of the Timoshenko section matrices for every foil. In the frame (X, Y, Z) (see Fig 3), the torsion Rz flexural rotation Rx are respectively associated to κ_1 and κ_2.

Table 9. Equivalent properties computed for the 4 experimental foils.

UD Orientation	$-50°$	$-30°$	$-10°$	$30°$
K_{11} [N]	1.91e+06	3.16e+06	5.14e+06	3.16e+06
K_{22} [N]	8.05e+05	8.26e+05	4.53e+05	8.26e+05
K_{33} [N]	7.65e+04	6.83e+04	6.56e+04	6.83e+04
K_{44} [N m^2]	6.18e+02	6.83e+02	3.55e+02	6.83e+02
K_{55} [N m^2]	3.36e+02	5.90e+02	9.52e+02	5.90e+02
K_{66} [N m^2]	1.13e+04	1.56e+04	2.90e+04	1.56e+04
K_{45} [N m^2]	1.03e+02	3.37e+02	2.14e+02	-3.37e+02

In Table 9, the axial and flexural stiffnesses K_{11}, K_{55} and K_{66} are decreasing when the fibers orientations are getting away from 0°, which is an expected behavior when studying composite materials. The torsional stiffness K_{44} is maximum for the UD orientation of $\pm 30°$. This structural behavior is also expected as Bishay and Aguilar, 2021 shows that the maximal torsional stiffness is reached for a fiber orientation of ± 25°.

To interpret the bend-twist coupling value K_{45}, it is relevant to develop the expression of the section torsion moment, from the Eq. 1:

$$M_1 = K_{14}\gamma_1 + K_{24}\gamma_2 + K_{34}\gamma_3 + K_{44}\kappa_1 + K_{45}\kappa_2 + K_{46}\kappa_3. \tag{26}$$

From Eq. 26, the torsion strain κ_1 is expressed as :

$$\kappa_1 = \frac{1}{K_{44}}(M_1 - K_{14}\gamma_1 - K_{24}\gamma_2 - K_{34}\gamma_3 \quad \underbrace{-K_{45}\kappa_2}_{\text{Contribution of the bending to the twist}} \quad -K_{46}\kappa_3). \tag{27}$$

Eq. 27 shows that for a BTC value $K_{45} > 0$, a negative flexion ($\kappa_2 < 0$) induces a positive torsion ($\kappa_1 > 0$), proportional to K_{45}. In the frame E (see Figure 2), the flexion is negative when the foil is bent upward. A positive torsion in the frame E corresponds to an upward displacement of the foil's leading edge, indicative of a nose-up deformation. In a FSI problem, such behaviors can be used to generate stable or unstable foils. A stable foil sees its angle of attack (AoA) decrease with increasing bending, while an unstable foil sees its AoA increase with increasing bending. Thus, in the present coordinate system, if $K_{45} > 0$, the foil is considered *unstable*. Indeed, if the foil is in a flow with a positive angle of attack, the hydrodynamic forces induce an upward deformation ($\kappa_2 < 0$), increasing the angle of attack due to the twist angle induced by the BTC ($\kappa_1 > 0$). The sign of the BTC define the *stability* of the foil and its magnitude the intensity of the additional torsion associated with BTC. Figure 12 illustrates, for the considered foil geometry, the relation between the orientation of the UD ply, the sign of the BTC and the *stability* of the foil.

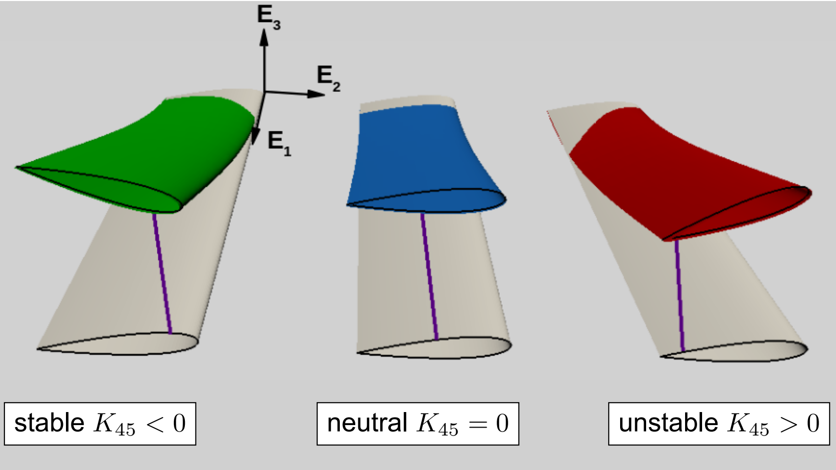

Figure 12. Illustration of the influence of fiber orientation on the *stability* of a foil.

5.2 Global Deformation: Influence of the Fiber Orientation

In this Section 5.2, experimental results are compared with numerical results, given by two finite element models, detailed in Section 4. As stated in this Section 4, *Abaqus 3D* and *Abaqus 1D* are respectively referring to the 2D/3D finite element analysis (FEA) and the equivalent beam model.

To validate the equivalent beam model for different UD orientations, the displacement of the corner of the clamping beam is studied experimentally and numerically for each foil and for 4 load cases that are given in Table 10. The positions of the mass are given in the coordinate system shown in Figure 13. In this frame, the position $(0.0, 0.0, 0.0)$ m corresponds to the leading edge of the foil at the clamping.

Table 10. Load cases considered to study the influence of the UD orientation on the foil mechanical behavior.

Load case	Position of the mass (X, Y, Z)	Mass [kg]
1	(0.1, 0.0, 0.5) m	5
2	(-0.6, 0.0, 0.5) m	5
3	(0.1, 0.0, 1.0) m	5
4	(-0.6, 0.0, 1.0) m	5

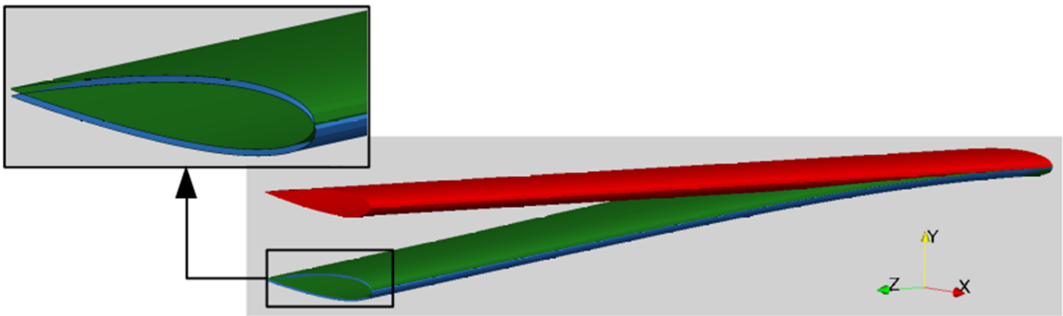

Figure 13. Comparison of the deformed foils computed with the two models for a UD orientation of -50° considering a suspended mass located at coordinates $(-0.6, 0.0, 1.0)$ m (Load case 4)– 🔴: Undeformed foil, (🔵) : *Abaqus 1D*, (🟢) : *Abaqus 3D*

Figure 13 shows the deformed shape for the foil with a UD orientation of -50° (most compliant foil) considering the fourth load case. Figure 13 is not scaled and illustrates the typical magnitude of deformation taken by the foils and it also highlights the good agreement between the two numerical models. In Figure 13, the two deformed foils are almost superimposed, which is encouraging for the future works, where FSI simulations will be performed.

The results given by the 3 models show a global good agreement. For instance, the displacement Dy computed by the 3 models for the load case 3 (in yellow in Figure 14) is maximum for the UD -50° and minimum for the UD -10°. This is consistent with the fiber orientations, as predicted in Table 5. For the load case 2, a positive displacement is computed by the 3 models, this is due to the positive torsion (Rz > 0, see Figure 16) of the foil which tends to bring up the corner of the clamping beam.

For UD -10°, Figure 14 shows that the experimental displacement measured by the GOM-SCAN is negative for the load case 4 whereas it is positive when computed with the numerical model. Two effects can be identified to explain this result. First, the experimental torsional stiffness is underestimated in the numerical models. Thus, for the load case 4, the experimental torsion Rz is smaller than the numerical torsion (see Figure 16). This induces a smaller experimental vertical displacement at the corner of the clamping beam, where the displacement is measured. The second effect is an overestimation of the flexural stiffness in the numerical models. This can be seen in Figure 15 which shows a smaller numerical bending rotation compared to the experimental one, this means that the foil is more deformed downward in the experimental case. These two effects explain the smaller vertical displacement Dy measured experimentally. To understand the differences in stiffness between the numerical and experimental model, a fine investigation of the foils' real structure should be performed. Indeed, the terms of the equivalent stiffness matrix (see Eq. 1) are very sensitive to the structural and geometrical variations, such as the orientation of the ply, its thickness or its elastic moduli.

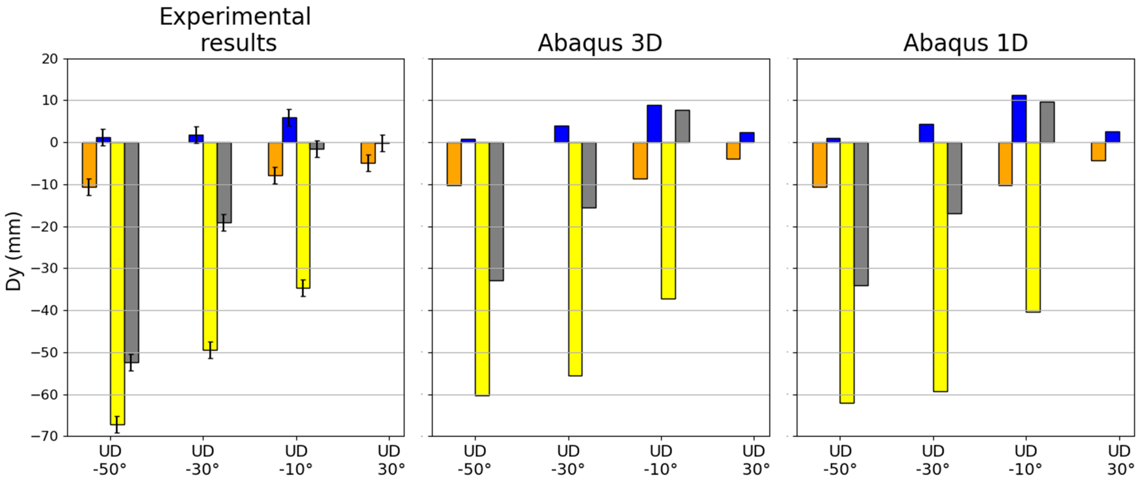

Figure 14. Displacement along Y of the corner of the clamping beam for the 4 foils and 4 load cases – (●): Load case 1, (●): Load case 2, (●): Load case 3, (●): Load case 4.

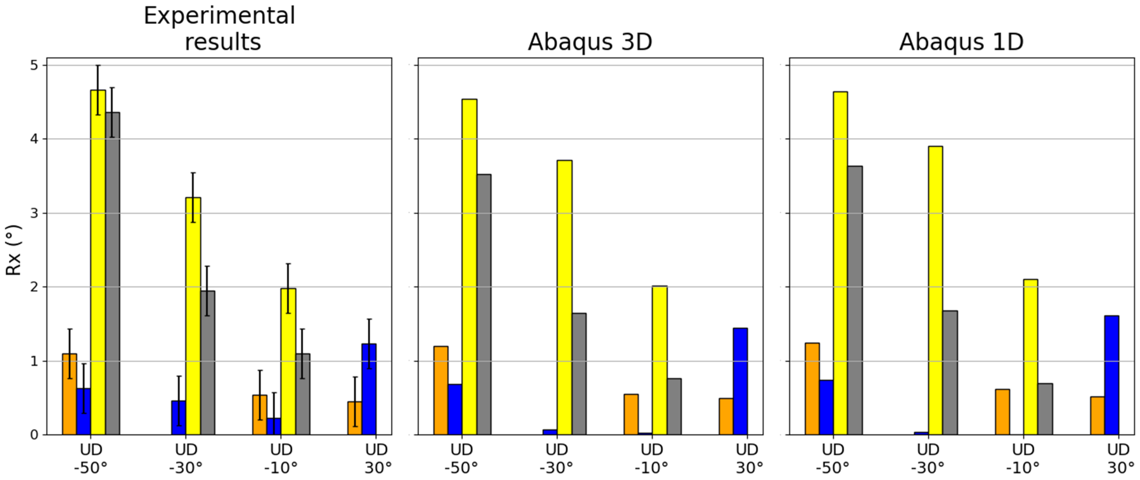

Figure 15. Rotation along X of the corner of the clamping beam for the 4 foils and 4 load cases – (●): Load case 1, (●): Load case 2, (●): Load case 3, (●): Load case 4.

The models also show a good agreement for the bending rotation Rx. For instance, Figure 15 shows that in the third load case, the rotation associated to the bending is getting smaller when the fiber orientation is getting closer to 0°. This result is obtained with the 3 models and shows that the flexion of the foils is correctly captured for each UD orientation. The values of the torsion Rz computed by the 3 models also show a good agreement. Figure 16 shows that the load cases 1 and 3, where the mass is located ahead the leading edge, induce a negative torsion whereas load cases 2 and 4 (where the mass is located after the trailing edge) induce a positive torsion. This structural behavior is expected and correctly captured by the 3 models. The torsion angles captured by the 3 models are also very close, the maximum difference between the experimental and numerical results is obtained for the third load case and the UD orientation of -10° (see Figure 16). In this case, the torsion magnitude measured experimentally is smaller than the torsion magnitude computed numerically. Figure 16 shows that the maximum differences between the torsions Rz computed experimentally and numerically occur for the load case 3 and 4, where the bending rotation Rx is the most important (see Figure 15). Thus, the difference between the numerical and experimental results is partially attributed to the numerical modeling of the BTC which is not perfectly representative of the behavior of the foils used during the experiments. These results show that the equivalent beam model correctly models the structural behavior of a foil for different UD orientations. In addition to this, the torsion is properly computed, which shows that the equivalent beam model can be used for FSI simulations.

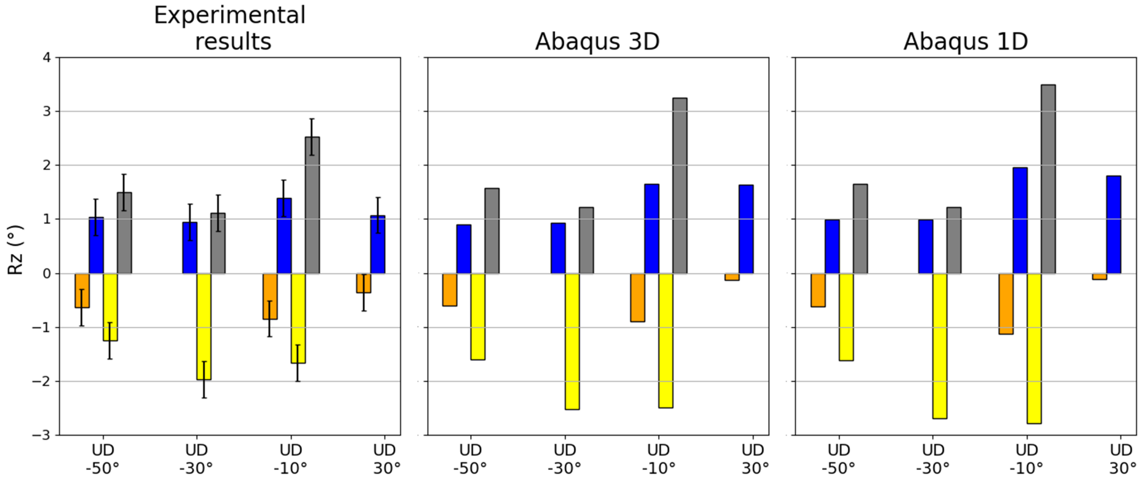

Figure 16. Rotation along Z of the corner of the clamping beam for the 4 foils and 4 load cases – (●): Load case 1, (●): Load case 2, (●): Load case 3, (●): Load case 4.

5.3 Global Deformation: Influence of the Torsion on the Bending

In this Section 5.3, the foils with the orientations 30° and -30° are retained because their BTC terms are of opposite signs. The objective here is to compare results obtained with the experimental setup, *Abaqus 1D* and *Abaqus 3D*. To do so, for each foil, 10 loading cases are considered where a 5 kg mass is suspended from the foil. In the considered load cases, the mass location along the span of the foil (Z) is fixed but its location along the chord (X) is variable. The Z component of the mass location is 0.8 m and its X component varies between -0.7 m and 0.2 m with a step of 0.1 m. Because the Z component of the mass location is fixed, the bending solicitation of a given foil is similar for every load case. The variable here is the torsion solicitation of the foil, which is directly linked to the X component of the mass location. For instance, if the mass is located ahead the leading edge ($X > 0$m), the loading induces a negative torsion whereas the induced torsion is positive when the mass is suspended behind the trailing edge ($X < 0.25$m). Because of the BTC, the torsions induced by the different load cases impact differently the bending of a given foil. The goal of these experiments is to capture the different bending behaviors for each load case and two opposite UD orientations. This is done to check the consistency of the BTC modeling in the numerical models.

The values of interest are Dy, Rx and Rz and their values are plotted in Figure 17 for the 2 UD orientations considered and several locations of the mass along the chord of the foil. To easily visualize the location of masses along the chord of the foils, the trailing and leading edges of the foils are plotted with black lines in Figure 17. The results show that the torsions captured with the 3 models are in good agreement, in terms of trend and magnitude.

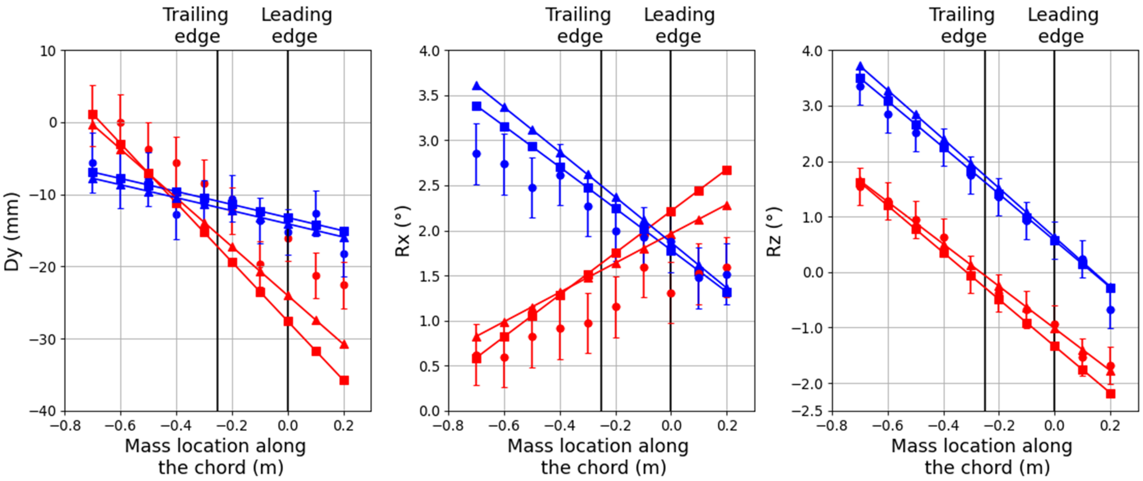

Figure 17. Displacement of the clamping beam corner for the foils 30° and -30° for different mass locations along the chord – (–▲–) : *Abaqus 1D* $-30°$, (–▲–) : *Abaqus 1D* $30°$, (–■–) : *Abaqus 3D* $-30°$, (–■–) : *Abaqus 3D* $30°$, (●) : *Experimental* $30°$, (●) : *Experimental* $-30°$.

For both UD orientations, the torsion decreases when the mass is moved from the trailing edge towards the leading edges of the foils. This behavior is expected and shows the ability of the equivalent beam model to capture the torsion of the foils for different mass locations. Because of the opposite UD orientations, the impact of the torsion on the bending is different for the UD orientations 30° and -30°.

In the present frame (see Figure 4), a negative Dy displacement is characterized by a positive value of Rx and a positive one is characterized by a negative value of Rx. Figure 17 shows that two different behaviors are captured for the bending rotation Rx. For the UD orientation of 30°, Rx decreases when the mass is shifted from the trailing edge towards the leading edge, whereas Rx increases for the orientation of -30°. This behavior, captured by the 2 models, shows that the BTC induced by the orientation of 30° tends to reduce the flexion of the foil when its torsion decreases. An opposite phenomenon is observed for the orientation of -30°, such behaviors are consistent with comments given in Section 5.1.

For the displacement Dy and the bending rotation Rx, the differences between the experimental and numerical results are higher than for the torsion Rz. Some of these differences are due to the uncertainties on the frame acquisitions. However, the trends of Rx and Dy are similar between the 3 models.

For the displacement Dy, when the mass is shifted towards the leading edge, the magnitude of the displacement decreases faster for the foil with the orientation of -30° than the foil with the orientation of 30°. This is consistent with the values of the bending rotation Rx because, for the orientation of -30°, Rx increases when the mass is shifted towards the leading edge, whereas it decreases for the orientation of 30°. Figure 17 shows that, for a UD orientation of 30°, the torsion of the foil stays positive when the mass is fixed ahead the leading edge ($X = 0.0$ m and $X = 0.1$ m). This is counter intuitive regarding the considered load case. This is caused by the BTC, where the negative flexion of the beam induces a positive torsion contribution. Thus, for a significant flexion, the positive torsion induced by the BTC can be higher than the torsion induced by the load case. The shift between the values of Rz for the 2 orientations in Figure 17 can be attributed to the torsion contribution induced by the BTC and the flexion of the foil. These results assess the capacity of the equivalent beam model to capture the BTC effects of foils with opposite UD orientations.

5.4 Local Deformation: Influence of the Mass Location

The objective is to validate the ability of the equivalent beam model to capture local phenomenon on the 3D surface of the foils. Because the strains are important near the clamping, a significant warping of the sections of the foils may occur. Therefore, to reconstruct the 3D surface of the foil, the warping is considered. This means that the motion of the points belonging to the 3D surface is decomposed into two components. Firstly, the surface follows a rigid body motion computed from the nodal displacements of the beam elements and the linear Timoshenko shape functions (see Section 2.2). Then, the deformation of the surface associated to the warping of the sections is computed. To do so, the deformed shapes of the sections of the foils are computed with the nodal displacements of the beam elements and the warping functions computed during the section analysis.

The results found with the GOM 5M are difficult to post-process because the computed displacements are small: around 0.01 mm. At this scale, the smallest error during the manipulation may invalidate the measure. The cleanest results given with the GOM 5M are obtained for the foil with the UD orientation of -30° and thus, this is the only foil considered in this Section. As in Sections 5.2 and 5.3, the displacements are computed by considering the foil with the clamping beam without hung mass as the reference configuration. This reduces the source of uncertainties due to the manipulation and the geometrical surface defects. For the foil with a UD orientation of -30°, the difference between the Z displacement in $Z = 0.27$ m and $Z = 0.35$ m (see Figure 9) is studied for two load cases. The load cases are chosen to maximize the deformations measured on the foil, they are defined such as:

- Load case 1: $X = -0.7$m and $Z = 0.8$ m;
- Load case 2: $X = 0.2$m and $Z = 0.8$ m.

In Figure 18 and Figure 19, the relative Z displacements between the ends of the speckle (see Figure 9) are respectively plotted for the load cases 1 and 2. For the two considered load cases, each of the 3 models gives similar results for the mean relative displacement between $Z = 0.27$ m and $Z = 0.35$ m. The relative Z displacement in the first load case is approximately 4 times smaller than in the second load case. This result is consistent with the results of Section 5.3. Indeed, for the orientation of -30°, Figure 17 shows that the bending rotation Rx is smaller for $X = -0.7$ m than for $X = 0.2$ m and the higher the bending rotation Rx, the higher Z displacement on the upper surface of the foil near the clamping. Thus, the relative Z displacement of the skin near the clamping is higher in the case where the mass is fixed ahead the leading edge of the foil. Figure 18 and Figure 19 show that this behavior is correctly captured with the 3 models. In Figure 19, the variation of the relative Z displacements along the chord measured with the 3 models are similar, it decreases near the leading edge of the foil ($X = 0$ m). There are still differences between the models, but their origins are hard to identify because of the uncertainties and the many unknowns (e.g. real shape of the foil, engineering constants, manufacturing defects, etc.). The precision of the 1D FEA in terms of trend and magnitude for the relative displacements is deemed sufficient and the results show that the equivalent beam model correctly captures the structural behavior of composite hydrofoils, even for local deformations.

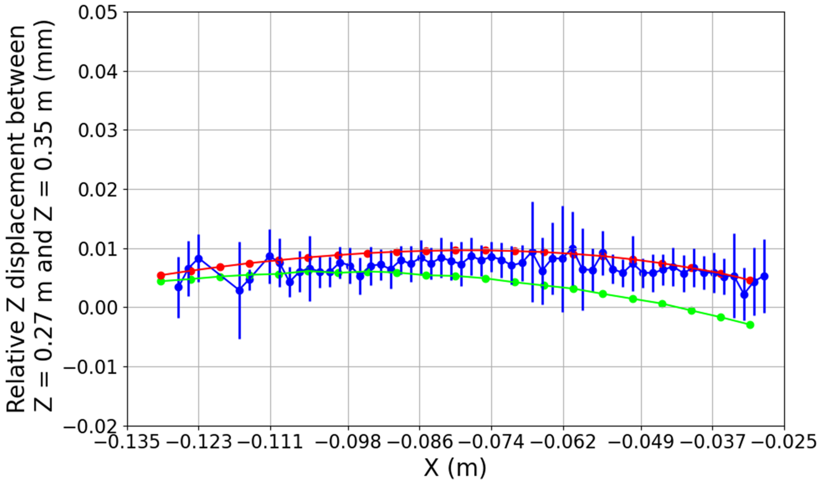

Figure 18. Relative Z displacement between $Z = 0.35$ m and $Z = 0.27$ m computed on the speckle area for a 5 kg mass suspended at $(-0.7, 0.0, 0.8)$ m – (●) : *GOM 5M*, (●) : *Abaqus 1D*, (●) : *Abaqus 3D*.

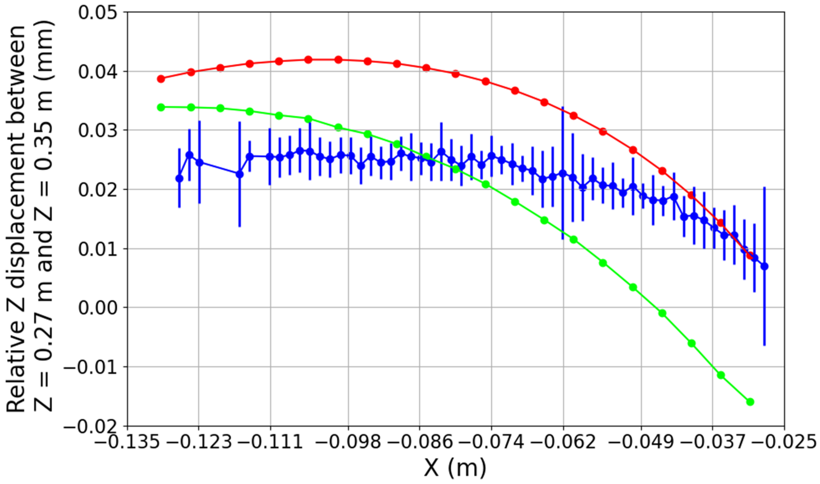

Figure 19. Relative Z displacement between $Z = 0.35$ m and $Z = 0.27$ m computed on the speckle area for a 5 kg mass suspended at $(0.2, 0.0, 0.8)$ m – (●) : *GOM 5M*, (●) : *Abaqus 1D*, (●) : *Abaqus 3D*.

5.5 Local Deformation: Warping Magnitude

To evaluate the impact of the warping on the numerical results, it is interesting to compare the warping of the section of a foil computed with the two numerical models. The warping cannot be computed from the results of the GOM 5M because the uncertainties on the displacement are of the same order as the warping displacement. To have readable results, the warping is only compared for the foils 30° and -30°. The warping is studied near the clamping ($Z = 0.27$ m) because this is where the deformations are the most important. The load case considered is a mass of 5 kg suspended from the foil at the coordinates $(0.2, 0.0, 0.8)$ m. The warping of the foils is computed with the upper part of the sections, this is acceptable because the geometry of the section is a symmetric airfoil. To compute the warping from the results given by *Abaqus 3D*, the displacement of the section of interest ($Z = 0.27m$) is decomposed into a rigid body motion component and a pure warping component. The first step of this decomposition is to identify the location of the shear center of the considered section in the initial and deformed 3D mesh, this gives us the rigid translation of the cross section. Then, the deformed section is transported onto the initial section. The rotation of the section is then determined as the rotation minimizing the distance between the points of the initial and deformed section, using the least square method. Finally, the residual displacements are identified as the warping. For *Abaqus 1D*, the warping displacement is computed from the warping functions with the functionality provided in Abaqus™ 2022.

In Figures 20, 21 and 22, every component of the warping displacement computed with the 2 models are plotted. The displacements are made dimensionless with the value of the rigid motion magnitude of the section. Figure 22 shows the out-of-plane warping of the sections of the foils with the orientation of 30° and -30°. The sign of the out-of-plane warping displacement is different between the foils, which is an expected behavior because the UD orientations of the considered foils are opposite. However, the warping magnitude is higher in the 1D model, which can partially explain the differences between the two numerical models in Figure 18 and Figure 19.

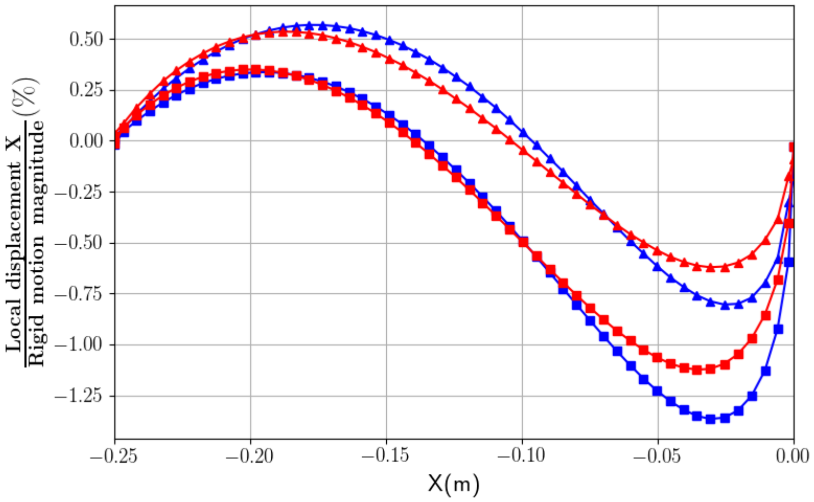

Figure 20. X component of the warping displacement at $Z = 0.27$ m for a 5 kg mass suspended at $(0.2, 0.0, 0.8)$ m – (–▲–) : *Abaqus 1D* $-30°$, (–▲–) : *Abaqus 1D* $30°$, (–■–) : *Abaqus 3D* $-30°$, (–■–) : *Abaqus 3D* $30°$.

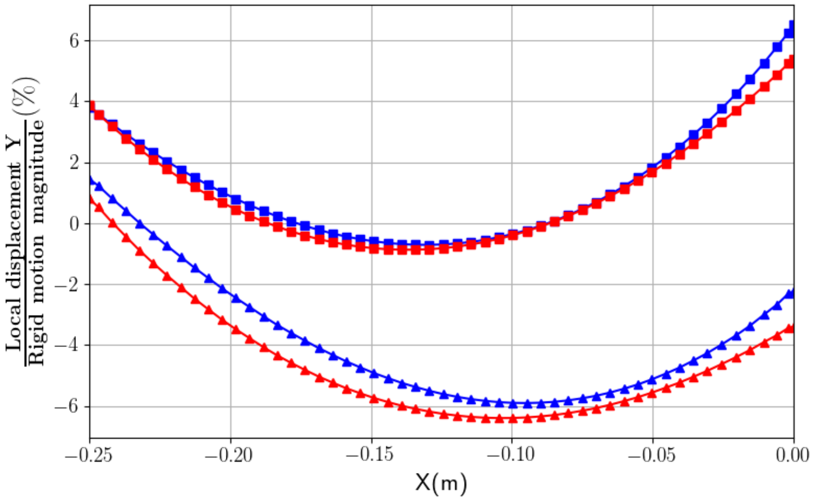

Figure 21. Y component of the warping displacement for a 5 kg mass suspended at $(0.2, 0.0, 0.8)$ m – (–▲–) : *Abaqus 1D* $-30°$, (–▲–) : *Abaqus 1D* $30°$, (–■–) : *Abaqus 3D* $-30°$, (–■–) : *Abaqus 3D* $30°$.

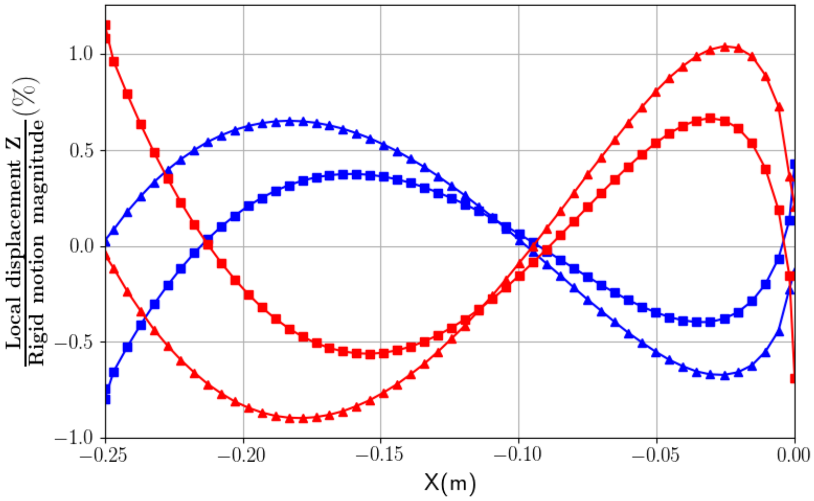

Figure 22. Z component of the warping displacement for a 5 kg mass suspended at $(0.2, 0.0, 0.8)$ m – (–▲–) : *Abaqus 1D* -30°, (–▲–) : *Abaqus 1D* 30°, (–■–) : *Abaqus 3D* -30°, (–■–) : *Abaqus 3D* 30°.

Figure 20 shows a good agreement between the two models in terms of trend for the warping displacements along X Dx^{warp}. According to both models, Dx^{warp} is smaller near the leading edge of the foil for the UD orientation of -30°. The two models estimate a maximum Dx^{warp} of about 1.2% of the rigid body motion, this is considered negligible. This is not the case for the warping displacement along Y, denoted Dy^{warp}. Figure 21 shows a warping displacement with a maximum magnitude of 6% for *Abaqus 1D* and *Abaqus 3D*.

The major differences between Dy^{warp} computed with *Abaqus 1D* and *Abaqus 3D* are inherent to the models. In *Abaqus 3D*, because the geometric nonlinearities are considered during the FEA, the internal forces in the shells impact the flexion of the foil. A stretched shell element sees its out-of-plane flexural compliance decrease (Reddy, 2006). For the considered foil, the skin of the foil can be locally considered as a plate borne elastically to the Airex web. The warping analysis is realized on the traction side of the foil and the traction is directed along the span of the foil. Thus, the magnitude of Dy^{warp} (out-of-plane flexion) is expected to be reduced. This phenomenon is observed because the FEA is realized considering the geometric nonlinearities. The magnitude of Dy^{warp} is smaller for *Abaqus 1D* because this model does not take this phenomenon into account.

This is due to the formulation of the section analysis, where the hypothesis of a warping smaller than the rigid body motion of the sections is made. The results show that the warping of sections should be modeled in the equivalent beam model to compute the strains, the stresses and the deformed shape of the foil, because its magnitude is not negligible regarding the rigid body motion. The warping computed with *Abaqus 1D* is almost correctly modelled, since its trend is correct, but its magnitude is overestimated compared to the warping computed with *Abaqus 3D*.

5.6 Stress Recovery

To end this work, a numerical comparison of the stress field in a section of the foil is performed. In *Abaqus 1D*, the 2D stress field in a section can be reconstructed from the warping functions and the sectional stresses of a beam element. This result is compared with the stress field given by *Abaqus 3D*. For this study, the most compliant foil is considered (-50°) with a 5 kg mass suspended to it at coordinates $(-0.6, 0.0, 1.0)$ m. The load is applied with the clamping beam and its mass is not neglected (3.54 kg). The deformed shapes of the foil computed with both models are illustrated in Figure 13. As in Section 3.2, to maximize stresses in the cross-section without being disturbed by the clamping, the studied section is located at $Z = 0.27$ m from the clamping.

The stresses are only studied in the composite skin of the foil because stresses in the web are negligible compared to the one in the skin. The analysis is conducted for the axial, transverse and shear stress components. In Abaqus ™, the axial stress is computed along the fiber direction (Dassault Systèmes, 2022).

Figures 23, 24 and 25 show the evolution of the axial, transverse and shear stress along the chord of the foil on its traction and compression side. The results show that the stress field recovered from the 1D FEA matches very well with the stress field computed in *Abaqus 3D*. This is true for both sides of the foils. Differences can be spotted between the numerical models for the taffeta ply. In *Abaqus 1D*, the magnitude of the axial stress is slightly higher than the one of *Abaqus 3D* (see Figure 23). However, Figure 13 shows that for the considered load case, the vertical displacement obtained with the equivalent beam model is also slightly higher. This partially explains the differences observed in Figure 23. This final study shows that *Abaqus 1D* is able to reconstruct a consistent stress field from the warping functions and sectional stresses of a beam element. The stress recovery could be included in a low-fidelity FSI coupling, to define a structural criterion informing us about the structural integrity of a given foil.

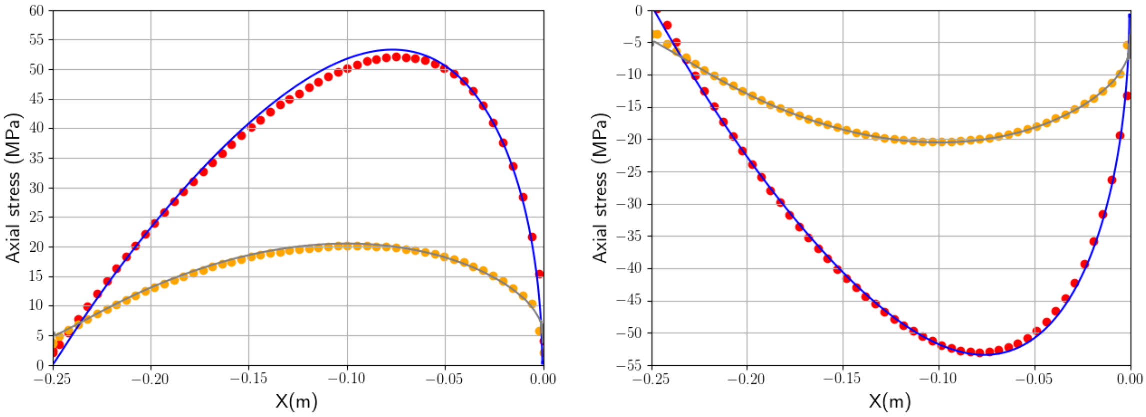

Figure 23. Comparison of the axial stresses computed numerically in the traction side (left) and compression side (right) of the glass plies of the foil, considering a UD orientation of -50° considering a suspended mass located at coordinates $(-0.6, 0.0, 1.0)$ m – (—): UD ply *Abaqus 3D*, (—):UD ply *Abaqus 1D*, (—): Taffeta ply *Abaqus 3D*, (—):Taffeta ply *Abaqus 1D*.

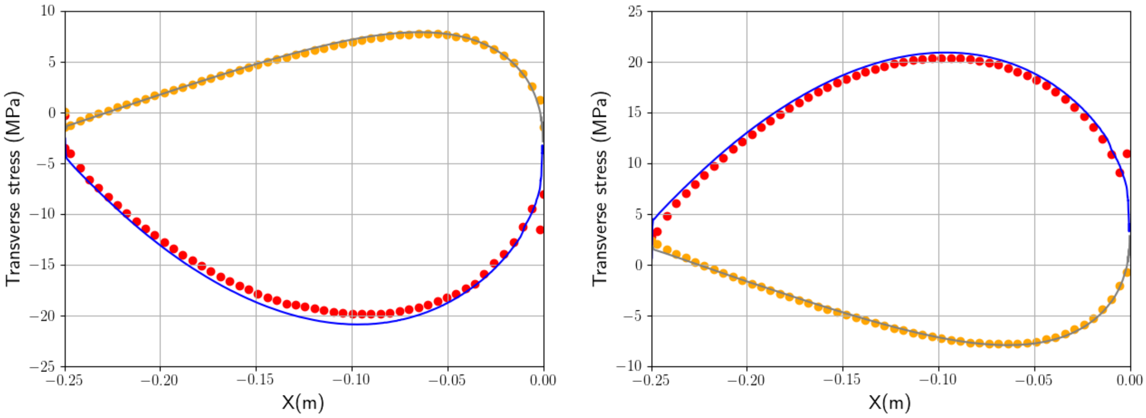

Figure 24. Comparison of the transverse stresses computed numerically in the traction side (left) and compression side (right) of the glass plies of the foil, considering a UD orientation of -50° considering a suspended mass located at coordinates $(-0.6, 0.0, 1.0)$ m – (—): UD ply *Abaqus 3D*, (—):UD ply *Abaqus 1D*, (—): Taffeta ply *Abaqus 3D*, (—):Taffeta ply *Abaqus 1D*.

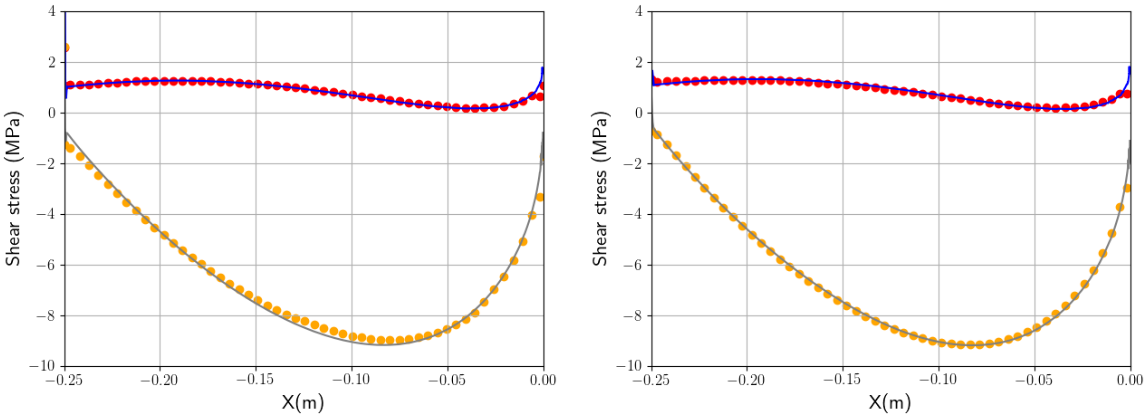

Figure 25. Comparison of the shear stresses computed numerically in the traction side (left) and compression side (right) of the glass plies of the foil, considering a UD orientation of -50° considering a suspended mass located at coordinates $(-0.6, 0.0, 1.0)$ m – (—): UD ply *Abaqus 3D*, (—):UD ply *Abaqus 1D*, (—): Taffeta ply *Abaqus 3D*, (—):Taffeta ply *Abaqus 1D*.

6 CONCLUSION

This paper presented a method to model a composite hydrofoil with equivalent beam finite elements. This work is conducted to determine if an hydrofoil could be optimized with FSI simulations considering the equivalent beam approach. This approach reduces the dimension of the optimization problem and the computational cost of its resolution. In the present study, the 1D finite element model is 50 times faster than the 3D finite element model, and this ratio goes up to 20 000 if the warping of the sections is neglected.

The equivalent beam modeling method is decomposed in two main parts, firstly, the sections of the foil are analyzed all along its span with the section analysis tools provided by Abaqus™ 2022. Then, from the results obtained with the section analysis, an equivalent beam is constructed as an assembly of 1D finite linear Timoshenko beam elements and a FEA is achieved for an arbitrary load case. The 3D geometry of the deformed foil is then determined from the equivalent beam displacements and the warping functions of the sections computed during the section analysis. The equivalent beam method is able to model couplings in the materials, such as bend-twist coupling or extension-twist coupling.

The equivalent beam model is validated by comparing the results given by an experimental campaign and a classical finite element analysis of the foil (3D solid + 2D shell finite elements). The experimental results are obtained with a GOM-SCAN and a GOM 5M, which are cameras respectively used to capture the global displacement of the foils and to study the local displacements of the foils near the clamping. The GOM-SCAN is used to characterize the general structural behavior of the foils for different fiber orientations and then, for a given flexion, the impact of the torsion on the flexion via the bend-twist coupling is investigated for two foils with opposite fiber orientations. The different results show a good agreement and validate that the equivalent beam model can describe a composite hydrofoil with anisotropic properties such as bend-twist coupling. With the GOM 5M, the local displacement of the upper surface of the foils near the clamping is measured and compared with the results of the numerical models. There is a good agreement between the experiments and the numerical model in terms of trend and magnitude. This shows that the equivalent beam model is precise enough to correctly capture local phenomenon on the surface of the foils. A numerical study of the warping magnitude is made to determine if it should be taken into account in the 1D finite element model. The results show that its magnitude is not negligible and therefore, it should be computed even if it increases the time of the structural computations.

The stress field in the warped sections can be computed from the equivalent beam model by Abaqus™. The stress recovery in the equivalent beam model is studied and shows that the stress field in the composite skin of the foil is consistent with the results of *Abaqus 3D*. This illustrates the capacity of *Abaqus 1D* to estimate the stresses in the section of a deformed foil, which is useful to define a structural criterion in a FSI simulation.

The method presented in this paper is new and was not validated to study composite hydrofoils. This paper shows that an equivalent beam model is able to model slender hydrofoils with couplings in the material. The results are encouraging and let us think that the equivalent beam model is adapted to realize FSI simulations on an hydrofoil to evaluate its performances. The main advantage of the beam model is its reduced computationnal time, which can be usefull to evaluate rapidly the performances of a hydrofoil in the early steps of an optimization process, where a multitude of designs are tested.

As a future work, computations should be performed considering a hydrodynamic loading applied on the foil, to validate the method for more complex load cases. The method presented in this paper should also be validated with more complex foils, with varying geometric and structural properties for instance. The next goal is to use the equivalent beam model to perform a topological optimization of a foil by varying its equivalent properties.

7 ACKNOWLEDGMENTS

The authors would like to thank the MASMECA technology platform who made the experimental campaign possible. We also thank Pierre Cocaign for his contribution to the experiments. Finally, we also want to acknowledge Benoît Augier of IFREMER Brest and Jean-Baptiste Marchand of the company Mabe surfboards for the manufacturing of the foils.

REFERENCES

Andersen, L. and Nielsen, S. (2023). Elastic Beams in Three Dimensions.

Balze, R., Roncin, K., Leroux, J., and Nême, A. (2017). Racing yacht appendages optimization using fluid-structure interactions. *The Fourth International Conference on Innovation in High Performance Sailing Yachts*. Lorient, France, pp. 51–57.

Bishay, P. and Aguilar, C. (2021). Parametric Study of a Composite Skin for a Twist-Morphing Wing. *Aerospace* 8, p. 259. DOI: `10.3390/aerospace8090259`.

Cella, U., Groth, C., Porziani, S., Clarich, A., Franchini, F., and Biancolini, M. E. (2021). Combining Analytical Models and Mesh Morphing Based Optimization Techniques for the Design of Flying Multihulls Appendages. *Journal of Sailing Technology* 6.01, pp. 151–172. ISSN: 2475-370X. DOI: `10.5957/jst/2021.6.1.151`.

Dassault Systèmes (2022). *Abaqus 2022 Documentation*. Available via the SIMULIA User Assistance suite. Dassault Systèmes Simulia Corp. URL: `https://www.3ds.com/products-services/simulia/products/abaqus/`.

Faye, A., Perali, P., Augier, B., Sacher, M., Leroux, J.-B., Nême, A., and Astolfi, J.-A. (2024). Fluid-Structure Interactions Response of a Composite Hydrofoil Modelled With 1D Beam Finite Elements. *Journal of Sailing Technology* 9, pp. 19–41. DOI: `10.5957/jst/2024.9.1.19`.

Feil, R., Pflumm, T., Bortolotti, P., and Morandini, M. (2020). A cross-sectional aeroelastic analysis and structural optimization tool for slender composite structures. *Composite Structures* 253, p. 112755. ISSN: 0263-8223. DOI: `https://doi.org/10.1016/j.compstruct.2020.112755`.

Giavotto, V., Borri, M., Mantegazza, P., Ghiringhelli, G., Carmaschi, V., Maffioli, G., and Mussi, F. (1983). Anisotropic beam theory and applications. *Computers & Structures* 16, pp. 403–413. DOI: `10.1016/0045-7949(83)90179-7`.

Hairer, E., Wanner, G., and Syvert P., N. (2008). *Solving Ordinary Differential Equations I : Nonstiff Problems*. Springer Series in Computational Mathematics. Berlin: Springer.

Han, S. and Bauchau, O. (2015). Nonlinear Three-Dimensional Beam Theory for Flexible Multibody Dynamics. *Multibody System Dynamics* 34. DOI: `10.1007/s11044-014-9433-8`.

Hodges, D. (2006). *Nonlinear Composite Beam Theory*. AIAA. ISBN: 978-1-56347-697-6. DOI: `10.2514/4.866821`.

Horel, B. and Durand, M. (2019). Application of System-based Modelling and Simplified-FSI to a Foiling Open 60 Monohull. *Journal of Sailing Technology* 4.01, pp. 114–141. ISSN: 2475-370X. DOI: `10.5957/jst.2019.4.1.114`.

Jorge, Z., Ronny, P., and Sotomayor, O. (2022). On the Digital Image Correlation Technique. *Materials Today: Proceedings* 49, pp. 79–84. DOI: `10.1016/j.matpr.2021.07.476`.

Lothode, C., Durand, M., Leroyer, A., Visonneau, M., DELAITRE, M., Roux, Y., and DOREZ, L. (2013). Fluid structure interaction analysis of an hydrofoil.

Mohammed Arab, F. (2020). Contrôle actif par pression interne des performances hydrodynamiques et de l'apparition de la cavitation d'un hydrofoil composite déformable en composite [*Active control by internal pressure of hydrodynamic performance and the appearance of cavitation of a deformable composite hydrofoil made of composite*]. PhD Thesis. UBO.

Nejatbakhsh, H., Ghasemi, A. R., Gharaei, A., and Najafabadi, H. (2023). An Analytical-Numerical Coupled Model for an Aeroelastic Analysis of Tail Flutter Based on Bending–Torsional Coupling. *Mechanics of Composite Materials* 59. DOI: `10.1007/s11029-023-10129-3`.

Ng, G. W., Yildirim, A., Youngren, H., Lamkin, A., Jonsson, E., and Martins, J. R. (2025). Design Optimization of America's Cup AC75 Hydrofoil Sections with Flaps. *Journal of Sailing Technology* 10.01, pp. 50–73. ISSN: 2475-370X. DOI: `10.5957/jst/2025.10.1.50`.

Oñate, E. (2013). *Structural analysis with the finite element method. Linear statics. Volume 2: Beams, plates and shells*. Vol. 2. Springer.

Reddy, J. N. (2006). *Theory and analysis of elastic plates and shells*. CRC press.

Sacher, M., Durand, M., Berrini, E., Hauville, F., Duvigneau, R., Le Maître, O., and Astolfi, J.-A. (2018). Flexible hydrofoil optimization for the 35 th America's Cup with constrained EGO method. *Ocean Engineering* 157, pp. 62–72. DOI: `10.1016/j.oceaneng.2018.03.047`.

Sacher, M., Leroux, J.-B., Nême, A., and Jochum, C. (2020). A fast and robust approach to compute nonlinear Fluid-Structure Interactions on yacht sails – Application to a semi-rigid composite mainsail. *Ocean Engineering* 201. DOI: `10.1016/j.oceaneng.2020.107139`.

Stäblein, A. and Hansen, M. (2016). Timoshenko beam element with anisotropic cross-sectionnal properties. *ECCOMAS Congress 2016*. Crete Island, Greece, pp. 7810–7819. DOI: `10.7712/100016.2377.9780`.

Tannenberg, R., Turnock, S. R., Hochkirch, K., and Boyd, S. W. (2023). VPP Driven Parametric Design of AC75 Hydrofoils. *Journal of Sailing Technology* 8.01, pp. 161–182. ISSN: 2475-370X. DOI: `10.5957/jst/2023.8.9.161`.

Temtching Temou, V. (2020). Etude expérimentale et numérique des interactions fluide-structure sur des hydrofoils flexibles en composite. PhD Thesis. UBO. URL: `http://www.theses.fr/2020BRES0043/document`.

Turnock, S., Keane, A., Bressloff, N., Nicholls-Lee, R., and Boyd, S. (2023). Morphing of 'flying' shapes for autonomous underwater and aerial vehicles.

Vanilla, T., Augier, B., and Paillard, B. (2021). Hydro-elastic response of composite hydrofoil with FSI. *Ocean Engineering* 221, p. 108230. DOI: `10.1016/j.oceaneng.2020.108230`.

Yu, W. and Blair, M. (2012). GEBT: A general-purpose nonlinear analysis tool for composite beams. *Composite Structures* 94, pp. 2677–2689. DOI: `10.1016/j.compstruct.2012.04.007`.

Yu, W., Hodges, D., and Ho, J. (2012). Variational asymptotic beam sectional analysis – An updated version. *International Journal of Engineering Science* 59, pp. 40–64. DOI: `10.1016/j.ijengsci.2012.03.006`.